EVIDENCE OF HYDROGEN BONDING, FERROELECTRICITY AND COESITE PHASE USING RAMAN SCATTERING AND DEVELOPING A RAMAN OPTICAL ACTIVITY INSTRUMENTATION

A Thesis

submitted in partial fulfillment for the degree of

Master of Science (MS)

as a part of the

Integrated PhD Program
(Material Science)

By
Priyank Singh

CHEMISTRY AND PHYSICS OF MATERIALS UNIT
JAWAHARLAL NEHRU CENTRE FOR ADVANCED SCIENTIFIC RESEARCH
BANGALORE – 560 064, INDIA
April 2016

DECLARATION

I hereby declare that the matter embodied in this thesis entitled "**Evidence of Hydrogen Bonding, Ferroelectricity and Coesite Phase Using Raman Scattering and Developing a Raman Optical Activity Instrumentation** " is the result of the investigations carried out by me in the Chemistry and Physics of Materials Unit, Jawaharlal Nehru Centre for Advanced Scientific Research (JNCASR), Bangalore, India, under the supervision of Professor Chandrabhas Narayana.

In keeping with the general practice of reporting scientific observations, due acknowledgements have been made whenever the work described is based on the findings of other investigators. Any omission which might have occurred by oversight or error in judgment is regretted.

_____

(Priyank Singh)

CERTIFICATE

I hereby certify that the matter embodied in this thesis entitled "**Evidence of Hydrogen Bonding, Ferroelectricity and Coesite Phase Using Raman Scattering and Developing a Raman Optical Activity Instrumentation** " has been carried out by Mr. Priyank Singh at the Chemistry and Physics of Materials Unit, Jawaharlal Nehru Centre for Advanced Scientific Research (JNCASR), Bangalore, India under my supervision and that it has not been submitted elsewhere for the award of any degree or diploma.

Prof. Chandrabhas Narayana
(Research Supervisor)

ACKNOWLEDGEMENTS

It is always a matter of great pleasure to acknowledge people who have inspired, motivated and supported me by sharing their knowledge and wisdom. I take this opportunity to extend my gratitude to all of them who had a great impact on my academic as well as personal life.

First of all, I had been extremely fortunate to get a wonderful mentor like Prof. Chandrabhas Narayana. I would like to thank him and convey my deepest sense of gratitude for providing excellent guidance through ample scientific inputs, enormous freedom in workplace and giving an exposure to wide variety of scientific problems. He has been very supportive in my professional as well as personal life. All this has been pivotal in making me a better scientist and a good human being. I have always admired his extraordinary energy and enthusiasm in every suggestion that he give.

I want to thank Prof. C. N. R. Rao for his never ending enthusiasm for science. He continues to be a source of inspiration for many of us.

I would like to thank all of my collaborators Prof Jayanta haldar (JNCASR), Dr. Divakara (JNCASR), Prof. N.C. Ghose, Prof. K.B.R. Verma and Ms. Nabadyuti berman (IISc, Bangalore).

I would like to thank the faculties of CPMU, TSU and EMU for their wonderful courses. I had many useful discussions with Prof. Swapan K. Pati and Meheboob Alam. I thank all of them.

I would like to thank Prof. L.D. Barron, Glasgow and Prof. Prasad Polavrapu, Vanderbilt who has been giving me very crucial inputs for Raman optical activity instrumentation. I greatly benefited from the inputs.

I had some amazing lab mates (past and present) like Drs Gayatri, Dhanya, Srinu, Partha, Sorb and Soumik and Shantanu, Rajaji, Divya, Priyanka and Jyotirmayee. We had lots of fun together and we have always learnt from each other. They have always kept the lab atmosphere a terrific place to work. I thank all of them.

I would like to thank my wonderful batch mates Mahima, Abhiroop, Nikita, Suchismita, Paramita, Amit and Saurav for making the stay comfortable and more scientific in discussions. I would like to thank my sister Disha, Shreya, Pratibha and Vaishali for her support and some of other friends Meenakshi, Zeenat, Sucheta, Srishti, Nancy and Jyoti for all the support during my hard times.

I express my heartfelt thank to all the academic, technical, library and computer lab staff members of JNCASR.

I have been very fortunate to be taught by many great teachers who value knowledge and wisdom equally. I thank all of them. I owe a lot to all of them. I would like to take this very special opportunity to thank my family specially my parents who has been very supportive despite of all the difficulties.

Dedicated to Cbhas and Alan Turing…

Contents

PREFACE

This thesis is unified more by the versatility of the use of inelastic light scattering (ILS) spectroscopy in different branches of science. The experimental investigations described in the resulting chapters each addresses discrete topics about different class of materials. Along with ILS, in order to understand specific material properties and open issues in these materials, the thermodynamic variable, namely temperature was used wherever necessary. The thesis consists of six chapters and is divided into two parts (Part A and B). Introduction to general aspect of inelastic light scattering, experimental details of Raman scattering, Temperature dependent measurements and application of Raman scattering to investigate hydrogen bonding interactions, temperature dependent Raman studies to confirm the ionic displacive polarizability in Te doped CCTO (calcium copper titnate) and Raman imaging of Himalayan rocks in part A. An attempt to succefully demonstrates the proof of principle of Raman optical activity is described in sixth chapter as Part B. Each chapter includes a topical introduction about the material under investigation.

Chapter 1 accounts a thorough introduction about the general aspects of inelastic light scattering (ILS). Classical and quantum approaches to describe the Raman scattering process are discussed. A brief discussion on Raman optical activity is included as last section in this chapter.

Chapter 2 describes about the experimental details of the design and working principles of Raman scattering setup. The methods of doing temperature dependent Raman experiments have also been discussed.

Chapter 3 contains the study of Te doped calcium copper titnate system to investigate ionic displacive polarizability using temperature dependent Raman measurements. The material shows three different transitions at low temperatures. In this chapter, role of Te^{4+}ions in the origin of displacive ion polarizability is elucidated using Raman spectroscopy.

Chapter 4 is about the role of hydrogen bonding in drug and lipid interactions. It is established that hydrogen bonding plays crucial role in these type of interactions using Raman spectroscopy.

Chapter 5 discusses investigation of Himalayan rocks using Raman Imaging. Coesite phase is established in sample and the thermodynamic conditions at the time of impact between indo Australian and Eurasian plates are predicted.

In **Chapter 6**, a successful attempt to fabricate the Raman optical activity (ROA) spectrometer is made. The proof of principle for ROA setup is demonstrated.

Chapter-1

Introduction

1.1 Light Matter Interaction

Light matter interaction is one of the most fascinating fields of physics. The light interacts in several ways depending on the properties of matter or the properties of light and such physics comes out. First we will consider the properties of matter.

1.1.1 Properties of matter

Band gap: The most important property of matter, which directs the light matter interaction, is its Band gap (E_g). Consider a photon with energy E incident on a material with band gap E_g. Following possibilities can arise: [1]

a) If $E_g = E$: In this case the photon is absorbed by the material creating an electron hole pair and is an efficient process.

b) If $E_g > E$: This case leads the photons to weakly interact with the material and pass through them as if it was transparent, which is termed as transmission.

c) If $E_g < E$: This criterion meets the strong absorption process.

Refractive index (n): This property of material can give rise to few more interesting types of light matter interactions, which can be classified as follows. [2]

a) $n > 1$**:** This type of materials slows down the speed of light with respect to the speed of light in vacuum, which gives rise to many fascinating phenomenon such as Refraction, Dispersion, total internal reflection etc.

b) $0< n <1$: In general, it is not possible but for X rays we find materials with absolute n lying between 0 and 1.

c) $n < 0$: Materials with negative refractive index are called metamaterials.

Now let's turn our attention towards the properties of light which can affect the nature of light matter interaction.

1.1.2 Properties of light

Polarization state: Light is an electromagnetic radiation and can be polarized with respect to its electric field. There are several types of polarization states possible for light; we can categorize them as follows: [3]

a) **Linearly or Plane polarized light:** The electric field of light waves are constrained in one plane.
b) **Elliptically polarized light:** Two electric field components with different magnitudes and phase difference.
c) **Circularly polarized light:** The two electric field components have same magnitudes and phase difference remains 90^0. They can be of two types; left and right circularly polarized light.

Optically active materials respond to the left and right circularly polarized light differently. Such interactions give important information about the Chirality of the matter.

One of the most dominant types of light matter interaction is known as **scattering** of light.

1.1.3 Scattering of light

This type of light matter interaction provides enormous amount of information about the matter, which has been the reason for physicists to be fascinated about this interaction. The subject of scattering of light has long and interesting history. Light scattering was a very popular research area in physics laboratories worldwide in the 1920s. The topic was under investigation by Lord Rayleigh in England, [4] Jean Cabannes in Paris, [5] Robert W. Wood in New York, [6] and Grigory Landsberg and Leonid Mandelstam in the Institute of Physics in Moscow. [7] Breakthroughs started with Lord Rayleigh who tried to explain the reason behind blue colour of sky. [4] Answering that question he came up with the classical theory of light scattering. These days it is well known as Rayleigh scattering, which is the process where the scattered photon and incident photon have same frequency (also known as elastic scattering). However, the first experimental evidence was given Tyndall, who observed that blue light is more strongly scattered than light of lower frequency and also noted that the scattered light was strongly polarized. [8]

It was in 1871, the first satisfactory explanation of even the most elementary aspects of scattering came from Lord Rayleigh who deduced his well-known λ^{-4} law for light scattering by objects whose dimensions are small compared with the wavelength of the

incident light. [4] Individual atoms, molecules and electrons, being such particles, scatter light elastically (i.e. without change in frequency) according to Rayleigh's law. In fact bigger particles such as dust particles also scatter light elastically, which is called Mie scattering. [9] Even Einstein and Smoluchowski gave the fluctuation theory to account for the variations in local dielectric constant which cause the scattering in otherwise homogeneous media. [10-12] By the end of 1920, there were many theories for inelastic scattering by particles. Following in the footsteps of Albert Einstein and Marian Smoluchowski, [10-12] Mandelstam developed a theory of light scattering at an interface that induced by fluctuations. [7] At the same time, Peter Debye published his theory about the specific heats of solids using the concept of propagating elastic waves in solids. [13] Before Mandelstam made the connection between the Fourier components in his theory and Debye's elastic waves; Leon Brillouin, [14] working independently in France, suggested that scattered light could be shifted in frequency and he calculated the spectrum of light scattered from a periodic, coherent fluctuations in the density of a liquid or solid. Later on, Adolf Smekal[15] developed the model for light scattering by a system with two quantized levels.

Even though the blueness of sky was satisfactorily explained by Rayleigh scattering theory; there were pending questions which remained unanswered such as marvelous blue of the Mediterranean Sea, It was generally believed that the blue color of the sea is due to the reflection of the sky as well as due to absorption of the light by the suspended matter in the water. Raman was the first to suggest that the blue color of sea is independent of sky reflection as well as absorption, [16-18] but rather it is due to the molecular diffraction. He investigated the scattering of light from liquids and to discover experimentally the scattering of light with change of frequency, which is now known as "Raman effect".

A short period after Raman published his work; there was a similar observation of light scattering with change of frequency in quartz reported by two Russian scientists, Landsberg and Mandelstam. [7] The Raman Effect emerged as a powerful tool for characterizing the materials. The inelastic scattering from sound waves, predicted by Brillouin, [14] known as Brillouin scattering, was first observed in quartz and liquids by

Gross. [19, 20] Brillouin scattering arises because of fluctuations in dielectric constant of medium. Raman and Brillouin scattering are treated similarly even though former arises because of fluctuations of molecular vibrations and later arise due to fluctuations in dielectric constant of the medium. The reasons for the division are largely historical, but in practice it turns out that there is a need for using different experimental techniques because of the different frequency regions probed. Today, the range of applications of light scattering in condensed matter is enormous and wide. After the advent of laser in 1960s, sophisticated spectrometers with associated electronics, inelastic light scattering spectroscopy has emerged as one of the most powerful and most widely used optical techniques for material characterization.

1.2 Raman Scattering

When light travels in a given medium, a very small fraction of it gets scattered by the inhomogeneities of the system. Fluctuations in the density of the medium that are associated with the phonons (quanta of the elastic wave which is outcome of collective atomic vibrations) are examples of dynamic scatterers, and they scatter light inelastically. Raman scattering is a process of inelastic scattering in which the incident photon with wave vector $\hbar k_i$ and energy $\hbar\omega_i$ is modified by interaction (creation or annihilation) with elementary excitations (quasi particles) of the matter leading to either an increase (anti-Stokes process) or a decrease (Stokes process) in the scattered photon energy, $\hbar\omega_s$, as well as a momentum, $\hbar q$, transfer to the matter. The elementary excitations could be any quasi particle such as optical phonons, surface and bulk polaritons, magnons, plasmons as well as electronic and vibrational excitations of isolated ions in crystals and molecular vibrations in liquids. In this thesis, we would be dealing with the lattice vibrations (phonons) which are the elementary excitation of interest described by their quasi-momentum $\hbar q$ and energy $\hbar\Omega$. Raman spectroscopy is very useful in identifying vibration modes (phonons) in solids (in molecules this particle is called vibron). The phonon frequency depends on the nature of chemical bond and the chemical constituents of the material. That simply tells us that Raman observables explores the molecular

picture of a system such as chemical bond strength, chemical constituents etc. It is evident that the bonding depends explicitly on the atomic distances, which predicts that applying perturbations (such as pressure, temperature, electric field, magnetic field etc.) to the system can be monitored directly by Raman spectroscopy. There are two robust mathematical theories of Raman scattering and the discussion of these theories is divided in subsequent subsections.

1.2.1 Classical picture of Raman Scattering

As a matter of fact light is an electromagnetic field. That simply means it has electric and magnetic field components. From Maxwell's relations we can deduce that $|E| / |B| = c$, which tells us that the strength of magnetic field is nearly 10^{-8} times the strength of electric field. This fact leads us to explain every light matter interaction is indeed the electric field and the matter interaction. When a photon is incident on crystal, the photon's oscillating electric filed (can be regarded as plane wave $E = E_0 e^{-i\omega t}$) induces polarization in the crystal. In the linear approximation, the induced electric polarization in any specific direction is given by,

$$P_i = \chi_{ij} . E_j \qquad \ldots\ldots (1.1)$$

where χ_{ij}, *is* susceptibility tensor of the crystal (in case of molecules it is polarizability tensor (α_{ij}) instead of susceptibility). The atomic vibration around equilibrium position leads to the susceptibility to change. Within the framework of classical electrodynamics the scattered light can be described as the oscillation of an ensemble of dipoles, the Raman scattering intensity can thus be expressed by the dipole radiation intensity using the transition susceptibility:

$$I_s = I_i \frac{\omega_s^4 V}{(4\pi\varepsilon\varepsilon_0)^2 c^4} |\hat{e}_s . \chi . \hat{e}_i| \qquad \ldots\ldots \quad (1.2)$$

Thus, for a particular vibrating mode (phonon) at a frequency, each component of the susceptibility tensor can be expressed as

$$\chi_{ij} = \chi_{ij}^{(0)} + \sum \frac{\partial \chi_{ij}}{\partial Q_k} Q_k + \frac{1}{2} \sum \left(\frac{\partial^2 \chi_{ij}}{\partial Q_k \partial Q_l} \right) Q_k Q_l + \; Higher\; Order\; terms \quad \ldots\ldots (1.3)$$

where $Q_j = Q_0 e^{\pm i\Omega_j t}$ shows normal coordinate of the vibration. From equation 1.3 we can get the expression of induced polarization (eq. 1.1):

$$P_i = \chi_{ij}^{(0)} E_{0j} e^{i\omega_i t} + E_{0j} Q_0 \sum \frac{\partial \chi_{ij}}{\partial Q_k} e^{i(\omega_i \pm \Omega_j)} + \frac{1}{2} E_{0j} Q_0^2 \sum \left(\frac{\partial^2 \chi_{ij}}{\partial Q_k \partial Q_l} \right) e^{i(\omega_i \pm \Omega_k \pm \Omega_l)} + \cdots \quad (1.4)$$

This expression corresponds to oscillating dipoles re-radiating light at different frequencies. On the right hand side, the first term corresponds to the Rayleigh scattering; the second term tells us one phonon Raman scattering and the third term suggest the two phonon Raman scattering and so on. It should be noted that the Raman scattered photons can have either high energy (anti-Stokes) or low energy (Stokes) than the incident photon. There are several additional phonon processes concerning influences by electric fields and deformation gradients. The radiated intensity of such oscillating dipoles is proportional to$\left| \frac{d^2 P}{dt^2} \right|$, so mathematically we have,

$$I_s \propto \omega_i^4 \left(E_{0j} \chi_{ij} \right)^2 + \omega_s^4 \left(Q_0 E_{0j} \frac{\partial \chi_{ij}}{\partial Q_k} \right)^2 + \ldots \qquad (1.5)$$

It is evident that the first term on right hand side account for the intensity of Rayleigh scattering and the second term shows the intensity of 1st order Raman scattering. For visible light $\omega_i \sim 10^{15}$ Hz, while the characteristic phonon frequencies are much shorter, typically $\Omega \sim 10^{12}$ Hz. Hence we can assume that $\omega_i^4 \approx \omega_s^4$ and the Raman scattering intensity goes asω_i^4.

$\frac{\partial \chi}{\partial Q} \neq 0$ is the criteria for the existence of the Raman activity in any material. In other words if a vibration causes a change in polarizability, it will be Raman active. It should

be mentioned that there can be vibrations which do not have change in polarizability, they are called *silent* modes. For local symmetries with a "centre of symmetry", an infrared active vibration is Raman inactive, and vice versa. This rule is usually known as the *mutual exclusion principle.*

The partial derivatives in Eq. (1.4) constitute the Raman polarizability ($\mathfrak{R}$), often termed as Raman tensor. For a first order one-phonon Raman process, is given by the complex second rank tensor:

$$\mathfrak{R} = \left(\frac{\partial \chi}{\partial Q}\right)_0 \hat{Q}_0(\omega_0) \qquad \ldots\ldots (1.6)$$

where $\hat{Q}_0$is a unit vector parallel to the phonon displacement.

The symmetries of the medium and of the vibrations involved in the scattering restrictions requirements on the Raman tensor. Due to the symmetry of the system the scattered radiation vanishes for certain choices of the polarization $\hat{e_i}$ and $\hat{e_s}$ and scattering geometries. These are the Raman selection rules. The scattering geometry is specified by four vectors: k_i and k_s (the directions of the incident and scattered light, respectively), $\hat{e_i}$ and $\hat{e_s}$ (the polarizations of the incident and scattered light, respectively). These four vectors define the scattering configuration usually represented as $k_i(\hat{e_i}\ ,\ \hat{e_s})k_s$ which is known as the Porto notation. [21]

1.2.2 Quantum picture of Raman Scattering

The classical theory fails in two aspects. One it is unable to explain the intensities of stokes and anti stokes Raman frequencies and second the influence of the symmetry of the medium. To understand Raman scattering process in quantum mechanical picture we must look at the energy level diagram for understanding the scattering process. Matter can be looked as a collection of several energy levels (called as electronic energy levels), out of these levels a few of them have longer lifetime and most of them have a very short lifetime (known as "not allowed" electronic energy levels). This leads to quantized energy levels in matter. Each of electronic energy level is coupled with quantized

vibrational energy levels and each of these vibrational energy levels is coupled with quantized rotational energy levels.

Any system is always in the ground state energy (E_g) configuration. When the photon ($h\nu$) is incident, the electrons get excited to higher energy level (E_v) such that

$$h\nu = E_v - E_g \qquad \ldots\ldots (1.7)$$

where E_v is the excited electronic energy levels.

After the electron is excited to higher energy state it usually comes back to ground state giving out the same energy. But one out of roughly 10^7 cases, the photon interacts with the phonons present in the system which leads energy exchange between them and hence the scattered photon has different energy. The process is shown in Fig 1.1.

At first sight it might look like that this scattering process can be described by a Hamiltonian involving photons and phonons only. However, the strength of such an interaction is very weak, unless the photon and phonon have comparable in energies. This is not the case for visible or ultraviolet light scattering. In fact the interaction between the photons and phonons is mediated by an electron. [22, 23] Feynman diagram is a very efficient way to represent a process (see Fig 1.1).

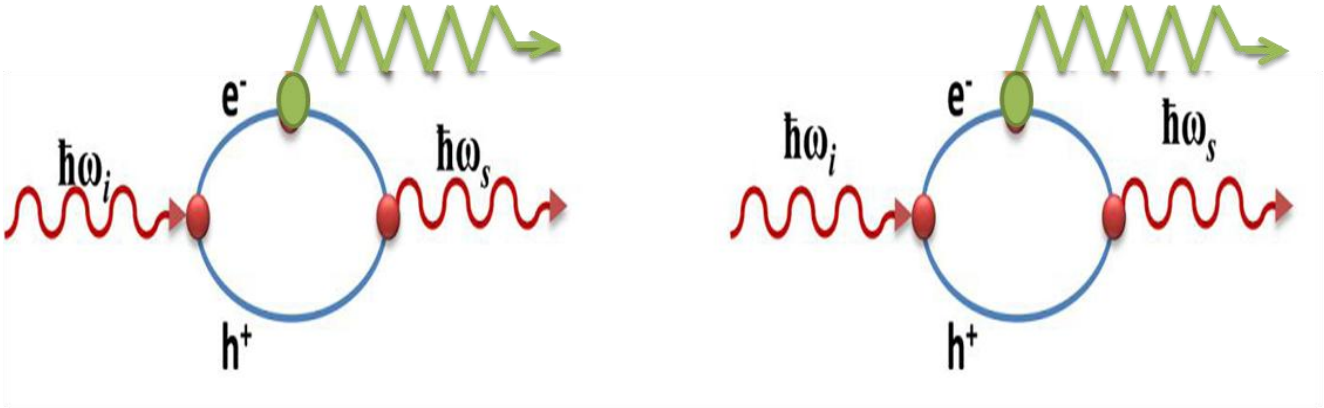

Figure 1.1: Feynman diagram for Stokes (Left) and anti-Stokes (Right)

The Raman scattering process consists of the following three major steps:

1. Photon-electronic system interaction - An incident photon excites the electrons from ground state |0⟩ into an intermediate (virtual) state |i⟩ by creating an electron-hole pair.
2. Electron-phonon or hole-phonon interaction- Due to creation or annihilation of a phonon in the lattice with energy $\hbar\Omega$, the intermediate state |i⟩ goes to another state |i'⟩, with lower or higher energy than the initial state |i⟩.
3. Electron –photon interaction, finally electron hole pair in the state |i'⟩ recombines radiatively to emit Raman scattered photon.

The process is depicted schematically in figure 1.2.

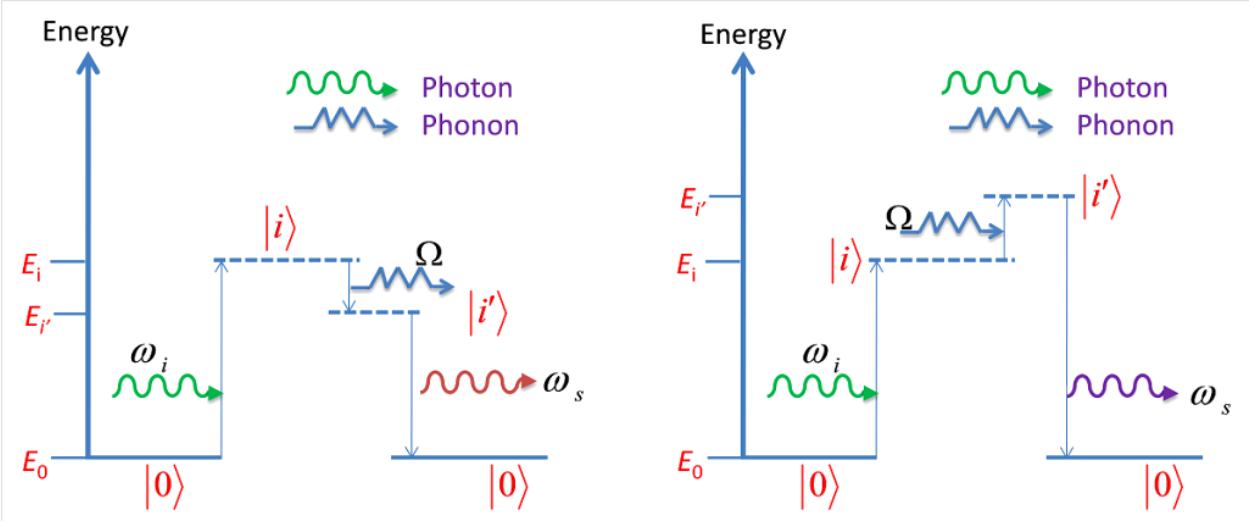

Fig1.2 - Schematic diagram of the energy states involved in Raman scattering (Left - Stokes process, Right- anti-stokes process)

The combination of these three interactions can be represented by the third order perturbation theory to give us the scattering cross section:[24]

$$\hat{e}_s \Re . \hat{e}_i \sim \frac{\langle 0|\hat{e_s}.p|i'\rangle\langle i'|H_{ep}|i\rangle\langle i|p.\hat{e_i}|0\rangle}{(E_{i'} - \hbar\omega_s)(E_i - \hbar\omega_i)} \qquad \ldots\ldots (1.8)$$

Here p is the electron momentum; H_{ep} is the electrons (hole)-phonon interaction Hamiltonian, E_i, $E_{i'}$, ω_s and ω_i are as defined in Fig. 1-2. The excited states shown in fig1.2 are not one of the energy eigenstates of the system. This makes Raman scattering a versatile tool, any photon source can be used to excite the system for getting phonon information of the system. But this leads to have very small value for electron phonon interaction Hamiltonian, which is why Raman scattering process is very weak (1 out of 10^7 photons scattered is Raman scattered). When the excited state happens to be one of the energy eigenstates then the scattering process is termed as Resonant Raman scattering. [23, 25, 26]

In the process of scattering, scattering cross section plays very important role to define how weak or strong a process can occur (with respect to other process). Raman scattering cross section is found to be very small, typically 10^{-30}cm^{-2}str^{-1}. We look at the standard deviation in differential Raman scattering cross section (which defines scattering efficiency) for scattering into specific angle $d\Theta$ and frequency increment $d\omega_s$, to understand the different aspects involved in physical measurement of Raman scattering process:

$$\frac{d^2\sigma}{d\Theta d\omega_s} = \nu V \frac{{\omega_s}^4}{c^4} |\hat{e}_s \Re . \hat{e}_i|^2 \langle UU^* \rangle_\omega \qquad \ldots\ldots (1.9)$$

here, $\Re$ is Raman tensor and U in the amplitude of elementary excitation, $\hat{e}_s$ and $\hat{e}_i$ are polarization vectors for scattered photon and incident photon, ν is interaction volume and V is volume of the sample. As inferred from basics of quantum mechanics $\langle UU^* \rangle_\omega$ is the power spectrum of U^2 with respect to different frequencies. Eq 1.9 has a crucial role in understanding the Raman scattering process, as it separates the differential scattering cross section into the shape factor $\langle UU^* \rangle_\omega$and the strength factor of the interactions$|\hat{e}_s \Re . \hat{e}_i|^2$.

Turning our attention to each of these factors, first looking at the shape factor; for one phonon Stokes scattering process we have;

$$\langle UU^* \rangle_\omega = \frac{\hbar}{2N\omega_i}(n_i + 1) g_i(\omega) \qquad \ldots\ldots (1.10)$$

And

$$\langle UU^{*}\rangle_{\omega} = \frac{\hbar}{2N\omega_i} n_i g_i(\omega) \qquad \ldots\ldots (1.11)$$

For anti-Stokes process.

where N is the number of oscillators present in the sample, n_i is Bose-Einstein factor for thermal population, $g_i(\omega)$ is line shape response function which in most of the cases takes the shape of

$$g_i = \frac{\Gamma_i/2\pi}{(\omega_i - \omega)^2 + (\Gamma_i/2)^2} \qquad \ldots\ldots (1.12)$$

which is equivalent to the Lorentz function. Hence Raman peaks are fitted using a Lorentzian function.

Above equations can be generalized for multi-phonon process by following up a little more math. [27, 28] Now we can visualize the Stokes and anti-Stokes Raman scattering process in following way:

"The Stokes Raman scattering occurs as a result of photon absorption from the ground state to a virtual state, followed by depopulation to a phonon-excited state. On the other hand, the anti-Stokes Raman scattering is a result of photon absorption from the phonon-excited state to a virtual state, followed by depopulation down to the ground state.**"**

In practice it is observed that the anti Stokes intensity of Raman spectra is far lesser than Stokes lines. Eq.1.4 predicts that the intensities (which is nothing but mathematical function of the pre-factor of second term) to be same in both cases. Invoking quantum mechanics we know that the probability of system in phonon-excited state is much less than the ground state, which can be explained by taking Boltzmann factor $e^{\frac{\hbar\omega}{k_B T}}$ into consideration. From above discussion we can say that:

$$\frac{I_{stokes}}{I_{anti-stokes}} = \frac{(\omega_i - \omega)^4}{(\omega_i + \omega)^4} e^{\frac{\hbar\omega}{k_B T}} \qquad \ldots\ldots (1.13)$$

From eq.1.13, knowing the intensity ratio of Stokes to anti- Stokes intensity for a particular Raman peak we can find the temperature of the sample. [29] It is interesting to note from equation 1.13 that stokes intensity increases and anti-stokes intensity decreases with increment in temperature. Another crucial remark about equation 1.13 is that it cannot be used in resonance cases as the equations in above analysis would change quite a lot. [30]

1.3 Raman Optical Activity (ROA)

Now we will invoke the polarization property of light photon. It is observed that in optically active media the refractive index for left circularly polarized and right circularly polarized light are different. This phenomenon is called optical rotation or optical rotary dispersion. It is observed that the difference persists in terms of absorption also, i.e. in an optically active medium we get different absorption of Left and right circularly polarized light (with different wavelengths). This observation was used to in IR measurements to enrich the sample information. Most of the work was done in late 1950s for polarization based IR measurements which was later named as Circular Dichroism (CD). [31] This special interaction led Barron to start looking at the difference in scattering of left circularly polarized light and right circularly polarized light (LCP and RCP). [32]

To explain the differences in such interactions we need to go beyond the electric dipole approximation to include contributions depending on the ratio of the molecular size to the wavelength of light (this ratio decreases as the wavelength of the light increases and vanishes for static fields). This suggests that in the semi classical treatment it is necessary to incorporate the electric dipole induced by the oscillating magnetic field and the electric field gradient of the optical wave, together with the oscillating magnetic dipole and electric quadrupole moments. In quantum mechanical treatment one needs more perturbation terms to incorporate these additional effects.

The theoretical background was set by Barron and Atkins in 1969. Here the theory of the polarization characteristics of Rayleigh and Raman scattering from chiral molecules which contained a new interference mechanism between light waves scattered via the polarizability and optical activity property tensors, leading to the prediction that the scattered light carries a small degree of circular polarization and the scattered intensity is slightly different in right- and left-circularly polarized incident light, was discussed. More robust approach was made in consequent papers by L.D. Barron, A.D. Buckingham in 1971, [32] where they defined a dimensionless entity circular intensity difference (CID) as an appropriate observable:

$$\Delta = \frac{I^R - I^L}{I^R + I^L} \qquad \ldots\ldots (1.14)$$

where, I^R and I^L are the scattered intensity for right and left circularly polarized light.

Raman optical activity is very small effect, [33-35] as Raman scattering process is intrinsically weak. Best possible values of Δ is of the order of 10^{-3}. Typical values of ROA scattering cross section is observed to be 10^{-4} fold weaker than Raman scattering cross section. This makes such observation more challenging. Furthermore the experiment is susceptible to artefactual signals, and several groups published ROA spectra that were spurious. In present work, there has been an attempt to develop a new setup for measurement of ROA in different molecules. Chapter 6 describes it in more detail.

Here we have successfully developed an ROA setup. The proof of principle will lead to developing a full-fledged ROA setup to address the problems in chemistry and biology.

References:

[1]. http://www.pveducation.org/pvcdrom/pn-junction/absorption-of-light

[2]. Richard P. Feynman, *Lectures on Physics* Vol.1.

[3]. http://hyperphysics.phy-astr.gsu.edu/hbase/phyopt/polclas.html

[4]. L. Rayleigh, *Phil. Mag* **41,** 447 (1871).

[5]. J. Cabannes, *Comptes Rendus,* vol. 160, pp. 62–63 (1915).

[6]. R.W. Wood. "Wavelength shifts in scattered light," *Nature* **122**, 349, (1928)

[7]. G. S. Landsberg and L. I. Mandelstam, *Naturwiss* **16,** 557 (1928).

[8]. J. Tyndall, *Phil. Mag* **37,** 384 (1869).

[9]. G. Mie, *Ann. Phys. , Lpz* **330,** 377 (1908).

[10]. A. Einstein, *Ann. Phys. , Lpz* **338,** 1275 (1910).

[11]. M. Smoluchowski, *Ann. der Phys* **330,** 205 (1908).

[12]. M. Smoluchowski, *Phil. Mag* **23,** 165 (1912).

[13]. Debye, Peter (1912). "Zur Theorie der spezifischen Waerme". *Annalen der Physik* (Leipzig) **39** (4): 789–839.

[14]. L. Brillouin, *Ann. Phys. (Paris)* **17,** 88 (1922).

[15]. A. Smekal, *Die Naturwissenschaften* **11,** 873 (1923).

[16]. C. V. Raman and K. S. Krishnan, *Nature* **121,** 501 (1928).

[17]. C. V. Raman, *Nature* **121,** 619 (1928).

[18]. C. V. Raman, *Indian J. Phys.* **2,** 387 (1928).

[19]. E. Gross, *Nature* **126,** 201 (1930).

[20]. E. Gross, Nature **126,** 400 (1930).

[21]. T. C. Damen, S. P. S. Porto, and B. Tell, *Physical Review* **142,** 570 (1966).

[22]. R. Loudon, *Advances in Physics* **50,** 813 (2001).

[23]. A. S. Barker and R. Loudon, *Reviews of Modern Physics* **44,** 18 (1972).

[24]. 15. M. Cardona, *Light scattering in solids I: Introductory concepts, Topics in Applied Physics, Vol 8, Springer-Verlag Berlin Heidelberg New York* (1982).

[25]. M. Cardona and G. Guntherodt, *Light-Scattering in Solids II: Basic Concepts and Instrumentation, Topics in Applied Physics, Vol 50, Springer-Verlag Berlin Heidelberg New York* (1982).

[26]. R. Loudon, *Journal de Physique* **26,** 677 (1965).

[27]. P. A. Temple and C. E. Hathaway, *Physical Review B* **7,** 3685 (1973).

[28]. B. A. Weinstein and M. Cardona, *Physical Review B* **7,** 2545 (1973).

[29]. M. Balkanski, R. F. Wallis, and E. Haro, *Physical Review B* **28,** 1928 (1983).

[30]. H. Herchen, M. A. Cappelli, M. I. Landstrass, M. A. Plano, and M. D. Moyer, *Thin Solid Films* **212,** 206 (1992).

[31]. P. Atkins and J. de Paula (2005). *Elements of Physical Chemistry* (4th ed.), Oxford University Press.

[32]. L. D. Barron and A. D. Buckingham (1971), Rayleigh and Raman scattering from optically active molecules, *Mol. Phys.* **20**, 1111-1119.

[33]. Lutz Hecht, Laurence D. Barron, Ewan W. Blanch, Alasdair F. Bell and Loren A. Day, Raman Optical Activity Instrument for Studies of Biopolymer Structure and Dynamics, *J. Raman Spectrosc*. 30, 815–825 (1999).

[34]. Laurence D. Barron , Lutz Hecht , Iain H. McColl & Ewan W. Blanch, Raman optical activity comes of age, *Molecular Physics,* 2006.

[35]. Laurence A. Nafie, Infrared and Raman vibrational optical activity: Theoretical and Experimental Aspects, *Annual Review of Physical Chemistry*, 1997.

Chapter-2

Experimental Techniques

In Light scattering experiments, we observe the spectral distribution of scattered light with respect to the spectrum of incident light. In the case of the Raman scattering the energy difference is very small (10-10000 cm^{-1}) and the intensity is many order of magnitudes smaller compared to incident beam. [1] Hence the Rayleigh scattered light should be suppressed efficiently. Monochromator and special filters help in recording the Raman scattering with high signal to noise ratio. Present chapter describes the spectrometer used for Raman spectroscopy and temperature dependent studies.

2.1 Raman Spectrometer

A custom built Raman setup is used for all investigations. An inexpensive, easy to build and high throughput micro-Raman spectrometer which is based on a single monochromator and a CCD detector coupled to a part of a Nikon microscope using a fiber optic cable is used. [2] Apart from the cost, this particular spectrometer provides enormous flexibility to carry out Raman experiments in ambient as well as in different temperature conditions with throughputs equally good as the commercially available spectrometers. The design, fabrication and working principle of the spectrometer are described in following subsections.

2.1.1 Design and fabrication of Raman microscope

In order to incorporate the issue of cost, flexibility and versatility in the design of the Raman microscope, the collection optics has been created by using a modular approach, where the focusing unit (LV-IM), double port (Y-IDP), sextuple nosepiece (C-N), universal epi-illuminator (LV-U EPI 2), eyepiece lens (CFI 10x) and a trinocular tube (Y-TF2) all from NIKON, Japan, is coupled. The collection optics is not a complete microscope, so it is mounted to the optical table using an L-shaped metal holder fabricated in-house. A schematic of the assembled micro-Raman spectrometer using the above mentioned microscope is shown in Fig. 2-1.

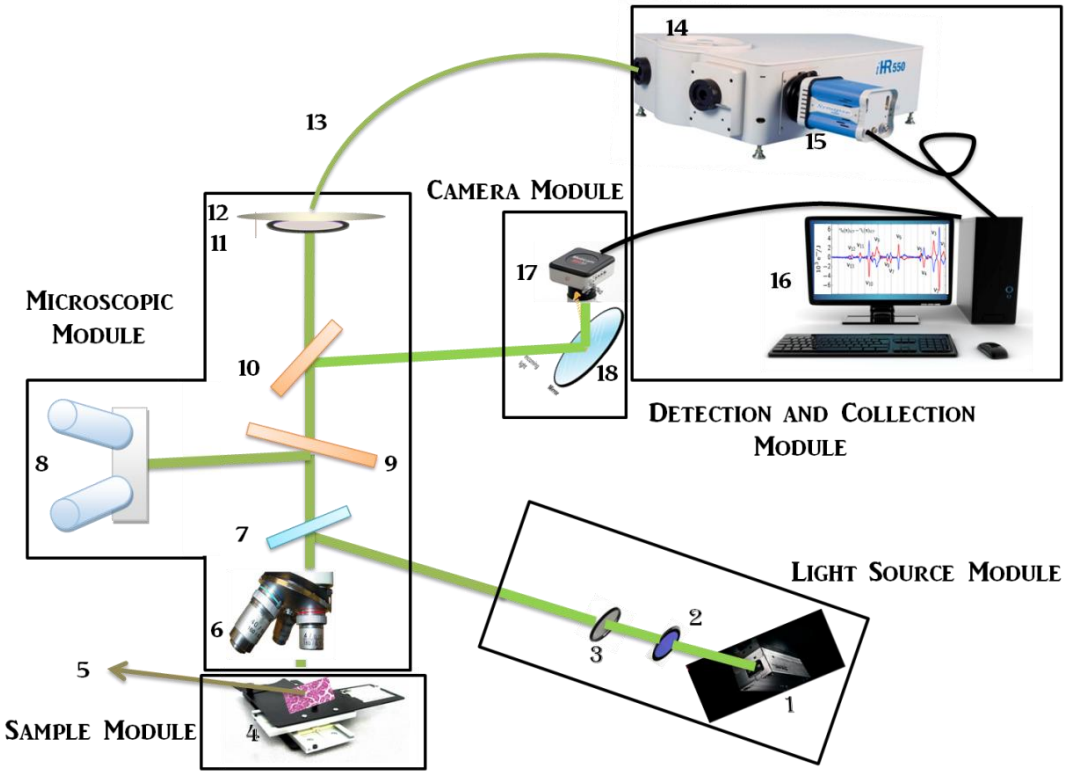

Fig.2.1: Schematic diagram of Raman Spectrometer. 1-laser light Source; 2- Band pass filter; 3- Neutral density filter; 4-Sample Stage;5-Sample;6-Objective lens; 7-Special Mirror; 8-Binocular; 9,10-Beam Splitter;11-Edge Filter; 12-Focussing lens; 13-Optical Fiber; 14-Spectrometer; 15-CCD; 16-Computer;17-Camera; 18-Mirror.

The laser is not completely linearly polarized and power of the laser is ~10 mW. The monochromatic, parallel laser beam is first passed through laser plasma-line filters (PF) (LL01-633-12.5, Semrock) to remove the laser plasma-lines. The high power density of the laser can sometimes result in damage of the chemical or structural properties of the sample; hence the beam then passes through one of several selectable neutral-density filters (NDF). These filters can be moved in and out of the beam path depending on the intensity requirement. The beam passes through the open field stop (FS) and the aperture stop (AS) of the microscope and hits the dichroic mirror (DM) or the special mirror (SM) at an angle of 45°. Both AS and FS serve as a guide to the optical path while aligning the laser into the microscope. The reflected laser beam is then directed onto the sample via an infinity corrected microscope objective lens (OL). The typical

objective chosen for most of the experiments was an infinity corrected 50X magnification objective with numerical aperture (NA) and working distance (WD) of 0.45 and 17 mm, respectively. Depending on the experimental requirement (depth of focus, working distance, scattering efficiency etc), the choice of the objective can be decided.

According to requirement, the sample and the focused laser spot (with all the NDFs engaged) can be observed at the eye piece by bringing the movable mirror 18 (fig 2.1) into the light path. Similarly, optical pictures can also be recorded by a camera (CAM) by engaging the movable beam splitter 10 (fig 2.1). Mirror 18 directs the beam to the camera (CAM) port (fig 2.1). The beam splitter splits the beam in 55:45 ratios and it is possible to record a spectrum as well as take a picture simultaneously. Even though, this will cause a 45% loss of Raman signal, it gives freedom to check if the sudden loss of Raman signal is due to the loss of laser alignment. The reflected and Rayleigh scattered light from the sample together with the inelastically scattered Raman signals are collected by the objective lens and directed onto the edge filter (EF) (LP03-532RS-25, Semrock) 11 (fig 2.1) which rejects most of the Rayleigh light. The collected light is then focused onto the optical fiber (13,fig 2.1) (200 μm multimode single core optical fiber with a band pass of 400–1000 nm) using an objective lens (NIKON L Plan 20X, 0.33 NA, WD 24 mm), as shown in the Fig. 2-1. The other end of the optical fibre was *f*-number matched to the monochromator (MONO) of focal length: 550 mm (Jobin-Yovn, Triax 550, Instruments SA, Inc., NJ, USA) attached with a liquid nitrogen cooled CCD (Spectrum One) detector 15 (fig 2.1). The monochromator (TRIAX 550) includes gratings: holographic 1800 grooves/mm, blazed reflection type 1200 grooves/mm (500 nm blaze) and 600 grooves/mm (450 nm blaze). This allows flexibility in the choice of the gratings for optimum resolution and desired spectral range. The on-axis triple grating turret, allows the TRIAX to maintain on-axis grating rotation during scanning, keeping a constant *f*-number and image quality. The light is focused onto the monochromator through a slit of variable width and dispersed by the motorized diffraction grating onto the CCD via a shutter. Before starting any experiment, the CCD was always liquid

nitrogen cooled to reduce the dark counts and to improve the signal to noise ratio. The CCD has rectangular two-dimensional array (1024 x 256) of pixels. A personal computer running the Labspec software program controls the data acquisition aspects of the spectrometer. Using the software the user chooses the desired grating and can also set the slit width, spectral range for the spectrum (determined by the angle of the diffraction grating), the exposure time of the CCD (controlled by the shutter) and the pixels used on the CCD for data collection. In this thesis, we have used these settings; the grating with 1800 grooves/mm with the input slit width of 100 or 200 μm. This provides us a resolution of ~ 0.7cm^{-1}.

As discussed in the beginning, this particular microscope doesn't include any sample stage. So the area under the objective lens is adaptable for use of different types of experimental setup. We use micrometer stages (MS) on which we place samples on a microscope slide for spectral acquisition at ambient conditions and focusing is done by the vertical movement of the stage. This also provides us tremendous flexibility and allows us to place our temperature controller, on this micrometer stages to do in-situ Raman measurements in different conditions of temperature. Fig. 2-2 shows a photograph of the fabricated micro-Raman spectrometer.

Fig. 2.3 shows the room temperature first-order Raman spectra of crystalline silicon at ~ 529 cm^{-1} recorded using this fabricated Raman microscope. [3] The excitation energy (2.33 eV) used in our Raman measurements is always greater than the band-gap energy of silicon (1.1 eV) so the laser light is strongly absorbed in the top layer of a silicon wafer. The spectra was collected using a 50X (NA = 0.80) objective. The input slit width was 200 μm and the 1800 grooves/mm grating was used. The laser power at the sample was 10 mW. As it can be seen, a very high signal to noise ratio is achieved.

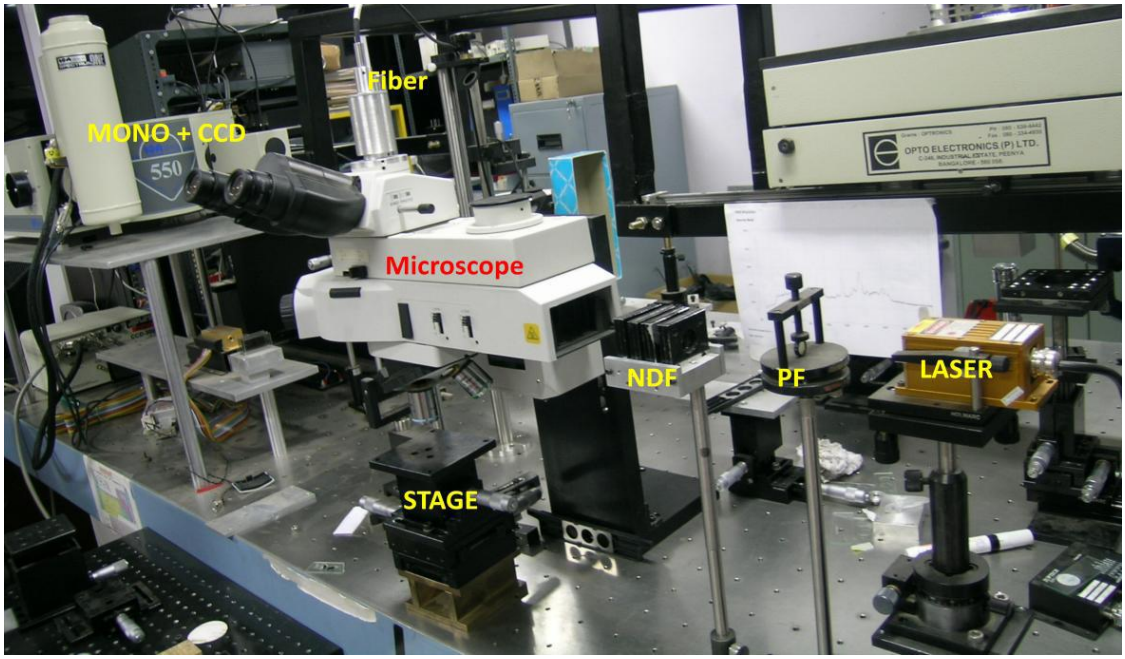

Figure 2.2: Photograph of the Fabricated Raman spectrometer.

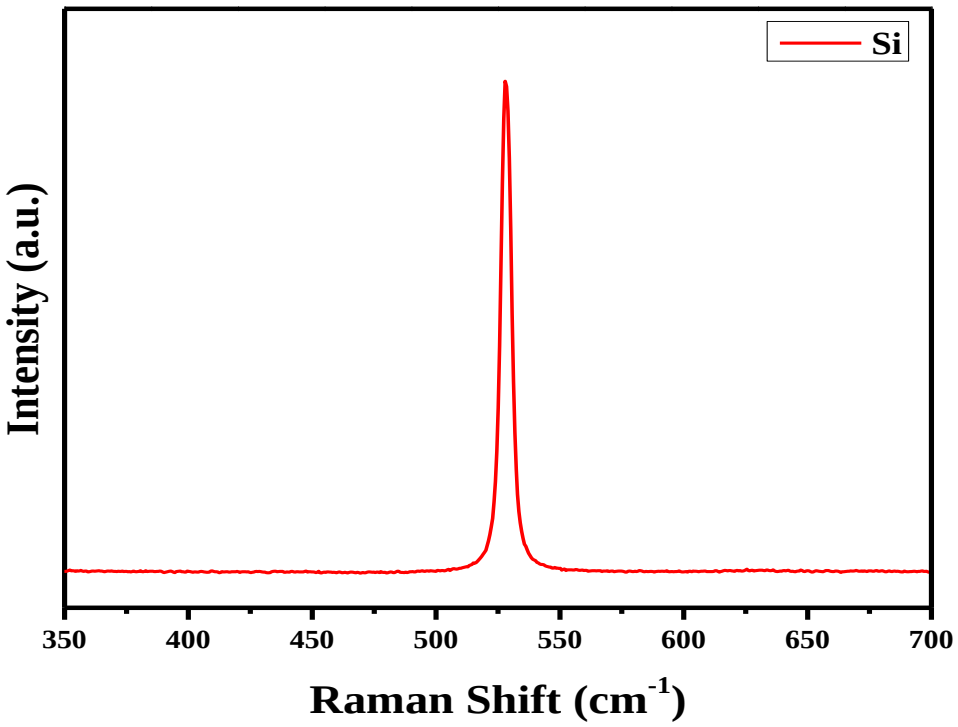

Fig. 2.2 Raman Spectra of Silicon wafer

The silicon wafer proved to be invaluable in the aligning of spectrometer optics on some occasion. The same piece of silicon wafer was always used for the purpose of quick calibration check. Another quick method of calibration is to check the peak arising due to emission line of mercury that occurs at 546.074 nm. This can be easily achieved by taking spectra with the room lights (mercury fluorescent tube) on. The accurate and exact calibration is always done using the emission lines of neon.

This spectrometer has some disadvantages. The use of edge filters (EF) does not permit the recording of the anti-Stokes part of the Raman spectrum. Furthermore, Rayleigh cut off frequency in these edge filters is large (>100 cm-1). So observing very low frequency modes is sometimes a problem. This problem can be circumvented by using a notch filter. In this set up we have used a dichroic mirror (DM535, NIKON) to reflect the laser light into the microscope objective. The use of dichroic mirror gives better throughput, but larger Rayleigh background at very low Raman shifts.

2.2 Temperature dependent studies

For temperature dependent Raman scattering studies, a cryostage (Linkam THMS 600, Linkam Scientific, UK) equipped with a temperature-controller (Linkam TMS 94) and liquid nitrogen pumping module (LNP 94) was used. The temperature was controlled with an accuracy of ± 0.1 K. The external control unit (Linkam TMS 94) maintains the set temperature and can also perform ramping up and down of the temperatures at user specified rates. We have used a ramp rate of 10°/min.

References:

[1]. W. Hayes, *Contemporary Physics* **16,** 69 (1975).

[2]. G. V. P. Kumar and C. Narayana, *Current Science* **93,** 778 (2007).

[3]. J. H. Parker, D. W. Feldman, and M. Ashkin, *Physical Review* **155,** 712 (1967).

Chapter-3

Triggering incipient ferroelectricity in CCTO ceramic through partial B-site doping by Te^{4+}

3.1 Introduction

In last decade, the use of perovskite oxide ferroelectrics has tremendously increased due to the diverse promising applications such as non-volatile ferroelectric memories, dynamic random access memories or tunable microwave devices. [1-3] However, a recent study of literature reveals a grown interest on $CaTiO_3$ or $SrTiO_3$ type of materials, which are known to be incipient ferroelectric material because of its tremendous application purpose. [4, 5] Generally, centrosymmetric ABO_3 type perovskite containing d^0 cataions at B-site i.e Ti^{4+}, Ta^{5+}, Nb^{5+}etc with polarizable BO_6 octahedra are classic examples of incipent ferroelectrics. [6-8] The tilt in BO_6 octahedra plays an important role in showing incipent behavior. Incipient ferroelectrics materials exhibit rise in permittivity (ε′) value of the material on cooling toward 0 K but saturate at low temperatures due to quantum fluctuations. [9] According to available literature, the dielectric and the structural properties of these materials are very sensitive to the inclusion of small amounts of dopants at A or B-site causing relaxor or ferroelectric behavior. [10, 11]

In cubic double perovskite $ACu_3Ti_4O_{12}$ family, Calcium Copper Titanate (CCTO, $CaCu_3Ti_4O_{12}$) was predicted to be incipient ferroelectric by Ferrarelli *et.al.* [12]. They showed that dielectric permittivity value associated with the bulk response decreases with increasing temperature for both CCTO single crystal and CCTO ceramic which is consistent with incipient ferroelectricity obeying the Curie-Weiss law with a negative Curie temperature. This result was adequately matching with the structure-property relationships observed in many other titanate-based perovskite with B-site octahedral tilting. The temperature dependence of ε′ and the Curie-Weiss behavior of a particular doping concentration of Mn^{2+} at A′-site (Cu-site) indicate the possible existence of incipient ferroelectricity in Mn-doped CCTO ceramics although the origin of incipient ferroelectricity is scarcely explained. [13] CCTO has attracted much of attention because of its high dielectric constant (~10^5), highest ever measured in nonferroelectrics over a wide range of frequency and temperature. It is a double perovskite with Im3 space group and T_h point group. In present investigations

Ti^{4+} is partially replaced with Te^{4+} ($5s^2$ lone pair) in CCTO, which can be abbreviated as CCTTO ($CaCu_3Ti_{4-x}Te_xO_{12}$). The partial doping at the B-site in CCTO resulted a different structure with centrosymmetric tetragonal (*I*4/*mmm*) crystallization with increase in the dielectric tunability of the material indicating existence of incipient ferroelectricity in the doped compound.

3.2 Experimental

CCTTO samples were provided by K.B.R Verma group at IISc. CCTTO is reported to crystallize in double perovskite structure with *I4/mmm* space group. [14] Ambient condition and temperature dependent Raman Spectra was recorded using the setup described in chapter 2.

3.3 Results and Discussions

Atom	Wyckoff position			Γ-point phonon modes
Ca1(2a)	0	0	0	$E_u + A_{2u}$
Cu1(2b)	0	0	0.5	$E_u + A_{2u}$
Cu2(4c)	0	0.5	0	$2E_u + A_{2u} + B_{2u}$
Ti(8f)	0.25	0.25	0.25	$3E_u + A_{1u} + 2A_{2u} + 2B_{1u} + B_{2u}$
Te(8f)	0.25	0.25	0.25	$3E_u + A_{1u} + 2A_{2u} + 2B_{1u} + B_{2u}$
O1(8h)	0.2892	0.2892	0	$E_g + 2E_u + A_{1g} + A_{2g} + A_{2u} + B_{1g} + B_{1u} + B_{2g}$
O2(16n)	0	0.1867	0.3218	$3E_g + 3E_u + 2A_{1g} + A_{2g} + A_{1u} + 2A_{2u} + 2B_{1g} + B_{1u} + 2B_{2u} + B_{2g}$
Raman Active Modes : $(3A_{1g} + 3B_{1g} + 2B_{2g} + 4E_g)$				
IR Active modes : $(12E_u + 7A_{2u})$				

Table 3.1- Phonon modes in CCTTO

As reporteded in the earlier communication, $CaCu_3Ti_{4-x}Te_xO_{12}$ crystallizes in the double perovskite structure with space group I4/mmm (D_{4h}) and contains two formula

units per primitive cell. [14] Analysis of I4/mmm (mm2) site symmetry (Table 3.1 and 3.2), $CaCu_3Ti_{4-x}Te_xO_{12}$ yields a total of 20 Γ –point phonons. In which total of 12 phonon modes ($3A_{1g}+3B_{1g}+2B_{2g}+4E_g$) are expected to be Raman active. These modes are assigned by following the earlier Raman reports on tetragonal I4/mmm crystal structure of AFe_2As_2 and Sr_2RuO_4 ($Sr_3Ru_2O_7$). [15, 16] The Raman spectrum for C-0 (pure CCTO) and C-2 (CCTTO) poly crystalline ceramic powder, obtained at room temperature is shown in Fig.3.1. A clear shift in the Raman spectra is observed from CCTO to CCTTO. Table 3.1 and shows the Raman modes and assignment of the C-2. Six pronounced peaks at 290, 346, 443, 508, 572 and 745 cm^{-1} are easily distinguishable for C-2 sample. The peaks at 290 (E_g), 443 (B_{2g}), 508(A_{1g}), 572(A_{1g}) cm^{-1} are due to rotational mode of TiO_6. The other octahedron anticipated at Ti position is TeO_6. The signature peak of TeO_6 rotation might be assigned 346 (A_{1g}or B_{2g}) and 745(B_{1g}) cm^{-1}. Multiple Peak fitting analysis of Raman Spectra of C-2 sample reveals some broad Raman peak, i.e. 290, 619 and 662cm^{-1}, which indicate that there is mixing of rotational and stretching mode for both the TeO_6 and TiO_6 octahedron. There are two other peaks revealed in Raman peak analysis at 482 and 455 cm^{-1} which are assigned to anti-stretching mode of Ti-O bond of TiO_5 units, which can be unambiguously related to off-center displacement of Ti in the octahedral structure. [19]

$CaCu_3Ti_4O_{12}$		$CaCu_3Ti_{4-x}Te_xO_{12}$ (x=0.2)	
Exp (cm^{-1})	Modes	Exp (cm^{-1})	Modes
292	F_g	290	E_g
445	A_g	346	A_{1g}/B_{2g}
453	E_g	443	B_{2g}
511	A_g	455	B_{1g}
575	F_g	482	B_{2g}/E_g
		508	A_{1g}
		572	A_{1g}
		745	B_{1g}

Table 3.2- Raman mode assignment of CCTO and CCTTO.

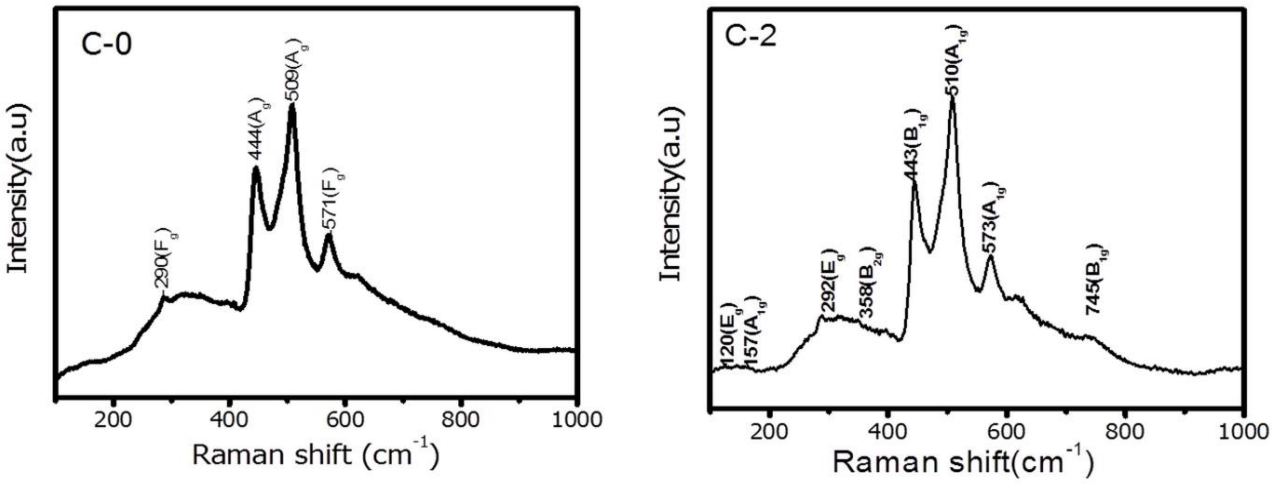

Fig.3.1- Raman Spectra of CCTO and CCTTO recorded at ambient condition.

The Raman mode frequencies in inorganic transition metal oxides are generally determined by the asymmetry, effective charge and bond lengths of participating atoms and atomic motions. Normally for perovskite materials, the modes involving heavy metals and rotational vibrations of metal-oxygen are found in the frequency range below 250cm^{-1}, the bending modes of metal oxygen lies in the range 200-500 cm^{-1}and stretching above 500cm^{-1}. As C-2 is also from the perovskite family, it could be predicted that the phonon modes below 250 cm^{-1} in C-2 Raman spectra are related to lattice modes involving Te vibrations. The peak with weak intensity at 147 cm^{-1} has E_g symmetry corresponding rotational vibration of TeO_6.

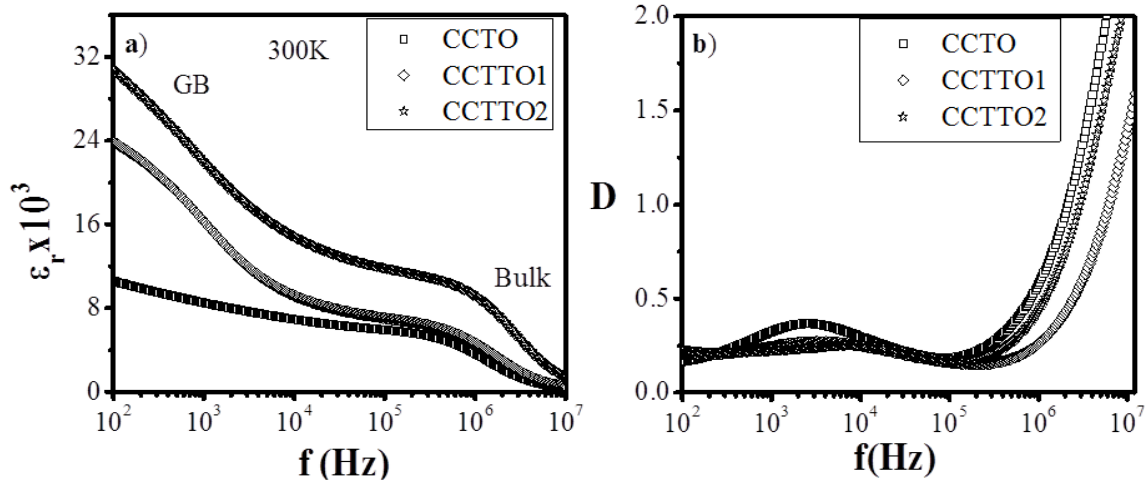

Fig. 3.2- Dielectric Measurements of different CCTO derivatives. (a) Dielectric permittivity; (b) Loss

As discussed above the effect of Te^{4+} substitution at Ti^{4+} on the structure of CCTO should be evident on the electrical behavior of the material. Fig.3.2a and 3.2b shows plots of the real part of dielectric permittivity (ε^*) and loss (D) vs frequency (f) at 300 K for undoped (x=0) and Te-doped (x=0.1, 0.2) CCTO ceramics. The doped samples (CCTTO) have permittivity (ε^*) value of ~2-3X 10^4 which is higher than that of undoped CCTO (~0.8X10^3) at 1 kHz. The well-known two distinguishable plateau of permittivity response with frequency corresponding to semiconducting grain(bulk) and insulating grain boundaries(GB) of pure CCTO are clearly conserved in Te doped CCTTO samples along with the prominent GB relaxation in the low frequency range (~10^3-10^4Hz) in doped samples. The high frequency corresponding intrinsic bulk permittivity (ε_r) (at 50MHz) is ~120 for CCTO, 190 for CCTTO1 (CCTTO with x=0.1) and 450 for CCTTO2 (CCTTO with x=0.2). The bulk and GB permittivity is higher for the CCTTO samples that the pure one.

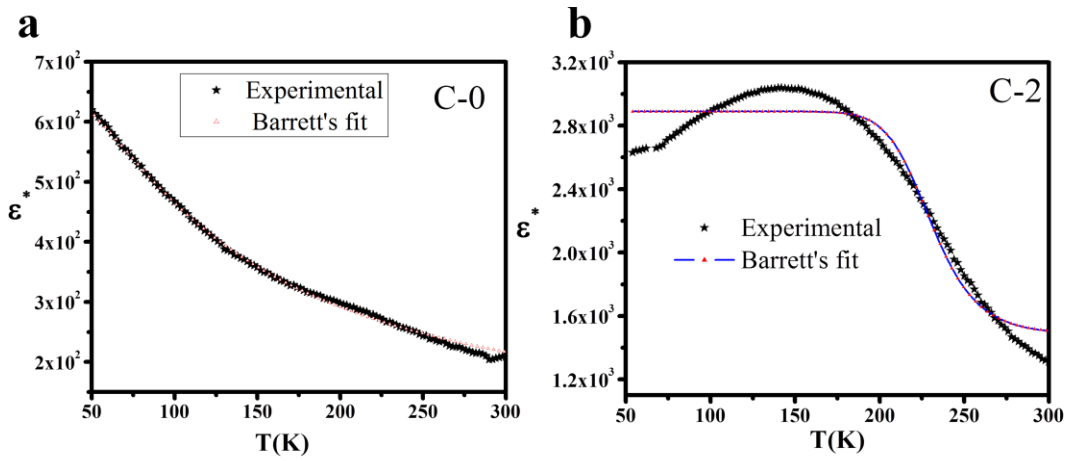

Fig. 3.3 Dielectric constant dependence on temperature of (a) CCTO, (b) CCTTO

Fig. 3.3a shows the variation of relative permittivity (ε_r) associated with the bulk response (at 1MHz) for different Te doping within the temperature range of 50-300K. For C-2 sample, the relative permittivity showed initially little increase followed by decrease after a dielectric maximum (at T_m) with increasing temperature (Fig. 3.3b). With doping concentration increase, the T_m shifts to higher temperature, for instance, the T_m for C-2 170 K. The pure sample C-0 show almost invariant behavior (with a little increase in permittivity) while decreasing the temperature. Dielectric behavior of

doped sample confirms polarization increase with the decrease temperature which is very similar to the anomalous dielectric behavior of incipient ferroelectric or low temperature ferroelectric in low temperature region (0-250 K).

In literature, there are several reports of enhancement of dielectric permittivity with A-site doping in CCTO with three common possible explanations such as; 1) A site disorder i.e. Ca-Cu antisite defects, 2) effective charge transfer between the 3D metals (Ti,Cu) leading change in chemical bonding of the metals ,3) displacive ionic polarization(Ti distortion in octahedra) in the unit cell leading to ferroelectricity. [17, 18] The structural investigations by XRD and TEM clearly indicate all the reported mechanisms could be plausible reasons in dielectric enhancement with Te doping in B –site. So we can discuss the structural consequences affecting the dielectric property in a thorough manner. We concentrate on the displacive ionic polarizability arising from locally stretched lattice resulting "rattling" cation in octahedral oxide cage.

Displacive ionic polarizability associated with Ti ion in pure CCTO has been proposed by C. Sinclair *et.al.*[18] The mechanism is investigated with the low temperature polarization enhancement (as a result of transition or ordering in metal-oxygen structural units) . This aspect can be understood by using temperature dependent Raman spectroscopy. Figure 3.4a shows the high frequency region (400-580 cm^{-1}) associated with internal modes of the TiO_6 octahedron. Most intense peak is at 515 cm^{-1} at ambient condition represents A_{1g} mode (symmetric stretching of TiO_6). Fig. 3.4b shows the external mode region (100-350 cm^{-1}). This region is related to the Ti^{4+}, Te^{4+} ion and its cooperative motion with oxygen over the whole lattice. We observe a new modes appear around 260 K related to TeO_6 lattice modes at around 246 cm^{-1} and 266cm^{-1}. Figure 3.4c shows the temperature dependence of A1g mode. It is seen that up to 260 K the mode shows very little temperature dependence, but at 260 K there is unusual hardening of the mode. The observation clearly suggest that Te^{4+} ion puts strain on the Ti^{4+} ion, and at 260 K it starts to release the strain leading to normal hardening of the mode. This could be the reason for an increased polarizability of CCTTO system and Te^{4+} facilitates higher ion polarizability.

In figure 3.4c we observe a change in temperature behavior of the A_{1g} mode around 210 K. At this point we also observe a softening of the 266 cm^{-1} mode due to TeO_6 lattice mode. The softening of 266 cm^{-1} mode continues till 120 K. Between 120 K-210 K A_{1g} frequencies is temperature independent. The 210 K corresponds to the T_m transition in the dielectric measurement shown in Figure 3.3b. Below 120 K, the 266 cm^{-1} modes stops softening and remains unchanged. In figure 3.4c the A_{1g} mode starts hardening abruptly after 120 K. It is interesting to see that the dielectric constant starts dropping below 130 K deviating from Barrett's fit. This could be due to decoupling of the Te^{4+} effect on Ti^{4+} leading to decreased ionic polarizability and hence decrement in dielectric constant.

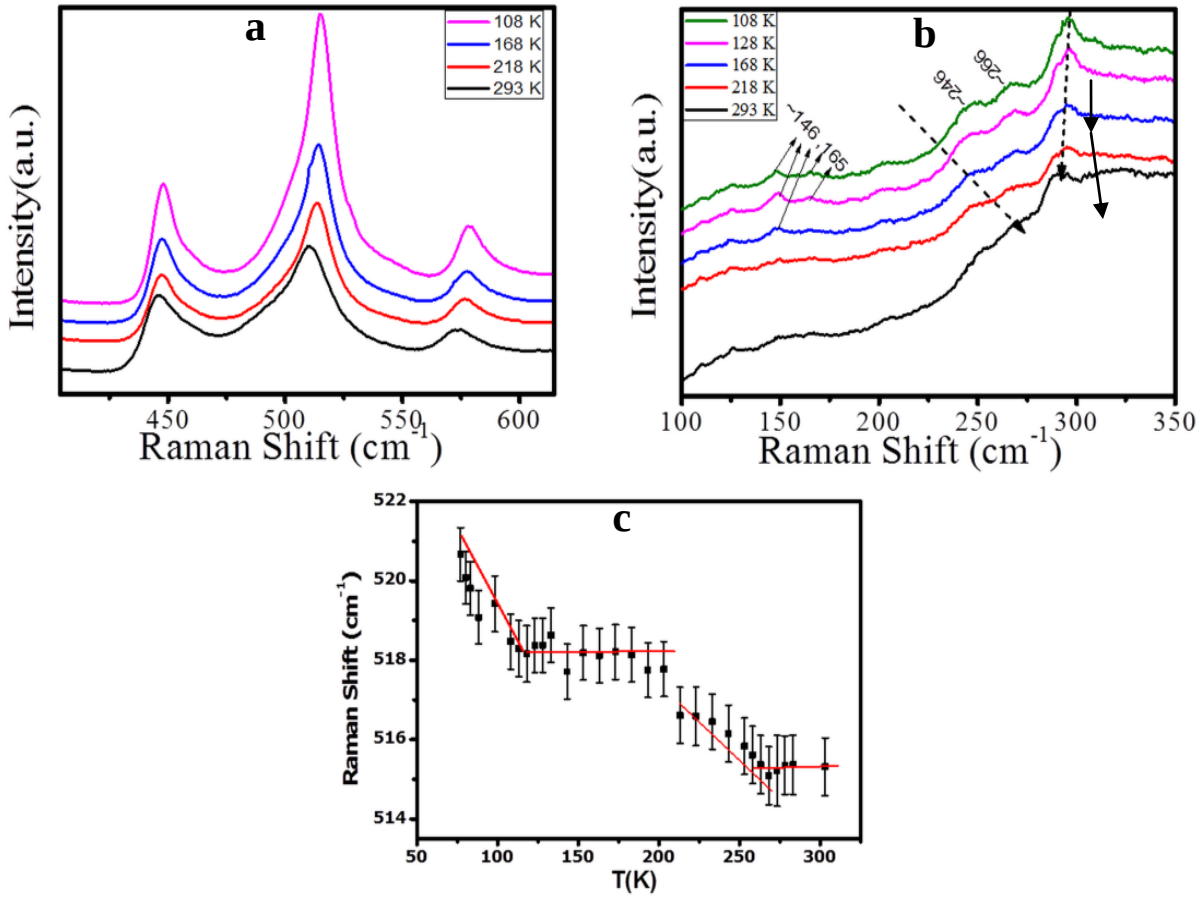

Fig 3.4 - Temperature dependent Raman measurement of C-2. (a) High frequency peak Hardening; (b) Low frequency peak hardening and softening; (c) Peak hardening of A_{1g} mode.

3.4 Conclusion

Temperature dependent Raman studies show that Te^{4+} doping induces strain in the TiO_6 leading to higher displacive ionic polarizability in CCTTO samples with increase in Te^{4+} doping. The Raman study is able to tell the microscopic origin of T_m transition in CCTTO due to the strong interaction of the Te^{4+} and Ti^{4+} sub lattices around 210 K. Beyond 120 K the two lattice decouple leading to decrease in dielectric constant.

References:

[1]. C.H. Ahn, T. Tybell and J.M. Triscone, *Appl. Phys. Lett.*, **75**, 856 (1999).

[2]. R. Guo, L. You , Y. Zhou , Z. Shiuh Lim , X. Zou , Lang Chen , R. Ramesh & J. Wang, *Nat. Comm.* **4,**1990 (2013)

[3]. J.F.Scott, *Science*, **315**, 954 (2007)

[4]. C. Cancellieri, A. S. Mishchenko, U. Aschauer, A. Filippetti, C. Faber, O. S. Barišić, V. A. Rogalev, T. Schmitt, N. Nagaosa & V. N. Strocov, *Nat. comm.*, **7** , 10920 (2016)

[5]. S. V. Aert, S. Turner, R. Delville, D. Schryvers, G. V. Tendeloo and E. K. H. Salje, *Adv. Mat.*, **24**, 523(2012)

[6]. F. A. Miranda, C. H. Mueller, G. A. Koepf and R. M. Yandrofski, *Supercond. Sci. Technol.* **8**, 755 (1995)

[7]. Yu. A. Boikov, Z. G. Ivanov, A. L. Vasiliev, I. Pronin, E. Olsson, and T.Claesson, *Appl. Phys. Lett.* **76**, 2708 (1995)

[8]. O. G. Vendik and S. P. Zubko, *J. Appl. Phys.* **82**, 4475 (1997)

[9]. O. E. Kvyatkovskioe, *Physics of the Solid State*, **43**, 1401 (2001)

[10]. **V.** Trepakovtt, F. Smutny, **V.** Vikhnin, V. Bursian, L. Sochava, L. Jastrabik and P Symikov, J. Phys.Cond.Mat., **7,** 3765 (1995)

[11]. V. V. Lemanov, A. V. Sotnikov, E. P. Smirnova, and M. Weihnacht, Appl. Phys. Lett. 81, 886 (2002)

[12]. M. C. Ferrarelli, D.C. Sinclair, A. R. West, H. A. Dabkowska, A. Dabkowski and Gr. M. Luke, J. Mater. Chem., **19**, 5916 (2009)

[13]. M. Li, A. Feteira, D. C. Sinclair and A. R. West, Appl. Phys. Lett., **91**, 132911(2007)

[14]. N. Barman, S. Tripathi, N. Ravishankar and K. B. R Varma, Centrosymmetric Tetragonal Tellurium Doped Calcium Copper Titanate and its Dielectric Tunability, (communicated).

[15]. A. P. Litvinchuk, V. G. Hadjiev, M. N. Iliev, B. Lv, A. M. Guloy, and C. W. Chu, Phys. Rev.B, **78**, 060503(R) (2008).

[16]. M. N. Iliev, V. N. Popov, A. P. Litvinchuk, M. V. Abrashev, J. Backstrom, Y. Y. Sun, R. L. Meng and C. W. Chu, ArXiv:cond-mat/0408432v1 [cond-mat.mtrl-sci] (2004).

[17]. M. C. Ferrarelli, D. Nuzhnyy, D. C. Sinclair and S. Kamba, Phys. Rev. B. , **81 ,** 224112 (2010).

[18]. R. Schmidt and D. C. Sinclair, Chem. Mater., **22**, 6 (2010)

[19]. E.A.V. Ferri , J.C. Sczancoski , L.S. Cavalcante , E.C. Paris , J.W.M. Espinosa , A.T. de Figueiredo , P.S. Pizani , V.R. Mastelaro , J.A. Varela and E. Longo, Materials Chemistry and Physics, **117,** 192 (2009)

Chapter-4

Raman investigations for understanding the Drug-Lipid interaction

4.1 Introduction

Mutation in viruses and other infectious biological entities gives rise to need for better antimicrobial agents with more efficient mechanism of action. [1, 2] In the past two decades, the focus towards the specific antimicrobial peptides (AMPs) which interact primarily with the microbial membrane increased a lot because of their ability to combat multi-drug-resistant microbes. [3-8] Combating the membrane has in fact shown low possibility of increment in bacteria resistance. [9] Above all the success in laboratories, there has been very limited success of AMPs in clinical applications due to their toxicity, low stability and high manufacturing cost which in turn prevent the large scale production. [3-5] There have been several approaches to overcome the cost issue and that led to develop diverse polymeric AMPs. [10-17]

Amphiphilicity is a key structural feature of AMPs. This allows AMPs to have proper balance of Hydrophobicity and cationic charge. It has been shown that the Amphiphilicity plays a key role in selective interaction of the polymers with bacterial membranes instead of mammalian membranes. [18] To be specific, electrostatic interactions bind the cationic polymers to the bacterial membranes that contain negatively charged phospholipids whereas the hydrophobic interactions facilitate the binding and the insertion into the lipid bilayers. It is a matter of fact that eukaryotic cell membranes generally contain a higher proportion of zwitterionic phospholipids and they are rigid and highly ordered due to presence of cholesterol. [18] Despite these differences only well studied interaction is electrostatic. Hydrogen bonding is the crucial and unexplored interaction in these cases.

In this work, we have investigated a few polymers using Raman studies to get the insight for understanding the role of hydrogen bonding the lipid and polymer interactions. Isosterically substituted ester (EC3P) and amide (AC3P) and lipid (DPPG) polymers were provided by Dr. Jayant Halder group (New Chemistry Unit, JNCASR). As a control the polymer HexP was taken which neither has ester nor amide functional group. This would not be able to have hydrogen bonding.

4.2 Experimental

Samples were prepared with 400 μgm per mL of methanol. With same concentrations a solution mixer of lipid and polymer was prepared. Glass slides with concave cavities were used for drop coating the samples. 20 μL sample was drop coated onto the glass slide and it was dried under vacuum in desiccators for 10 minutes. Measurements were performed using WiTec Raman Spectrometer (UHTS600 SMFC) equipped with CCD (CCD-17531) and aligned in backscattered geometry. The excitation source was 532 nm laser (Coherent Lasers make). Almost 20mW laser power was used to excite the sample. A 60x objective (Nikon make) with NA 0.8 was used for room temperature Raman measurements. A 50X ultra long working distance objective (Nikon make) was used for temperature dependent measurements. The typical accumulation time for each spectrum was 600s. Temperature dependent Raman measurements were performed using Linkam cryostage (Linkam Scientific instrument) and TMS temperature controller.

4.3 Results and Discussions

Fig 4.1 depicts the structures of polymers and the lipid involved. The main structural difference among polymers arises at the nitrogen site of imine group. In HexP there are no functional groups attached whereas in amide and ester we have $–CONH_2$ and –COOR groups attached. It is evident that there are two positive nitrogen atoms available in amide polymer (AC3P) but only one in ester polymer (EC3P). Similarly AC3P has 3 oxygen sites available for hydrogen bonding but in case of EC3P, it is four. Lipid (DPPG) has phosphate group as the primary source for hydrogen bonding interactions with polymer.

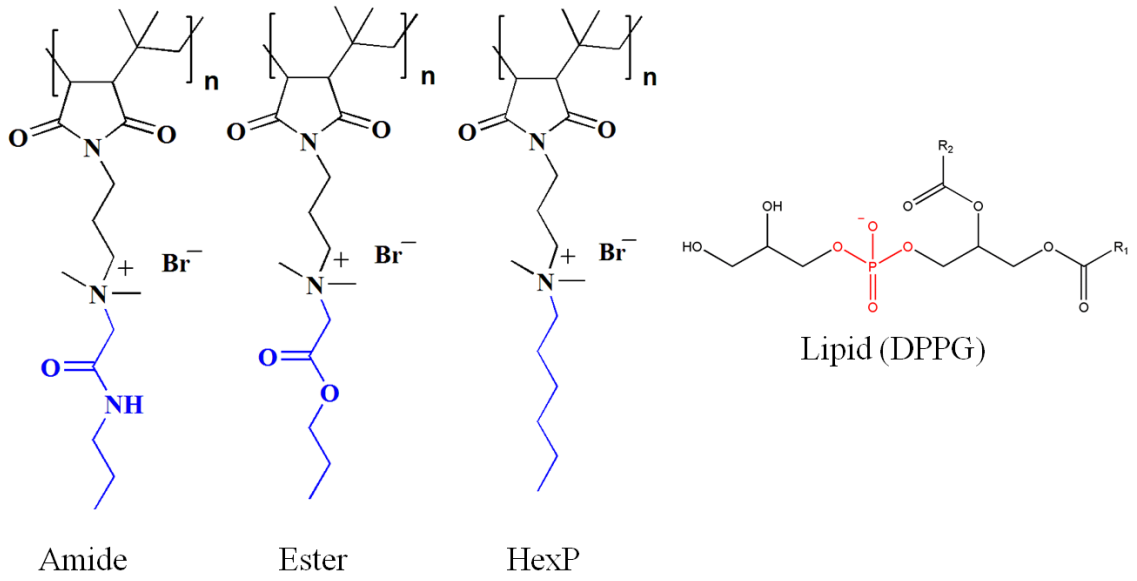

Fig. 4.2- Structures of Polymers and Bacterial Lipid

Fig.4.2 includes the full Raman spectra of individual chemical entities (polymers and lipids). As it is mentioned in the experimental section that the drop coated region is dried well, so the interference from methanol in Raman spectra was avoided. It is evident from Fig. 4.1 that there are several methyl groups present in all the chemical entities under investigation; which is reflected in Raman spectra as a very strong peak in the range of 2800- 3000cm^{-1}. Since our interest is in the specific interaction of hydrogen bonding between the lipid and the polymer, we look at the moieties which have highest possibility for such interactions.

For concentrating on specific interaction (hydrogen bonding) of polymers (AC3P, EC3P, HexP) with the bacterial lipid (DPPG), we focus on the modes related to the phosphate region of the lipid (1040 - 1150 cm^{-1}), the amide (-CONH-) and the ester (-COO-) regions in the polymers (1600-1800 cm^{-1}). As shown in Fig. 4.3A, 1064 cm^{-1} vibrational mode is due to -P-O-(DPPG head group), 1100 cm^{-1} is due to PO_2^- and 1129 cm^{-1} is due to -P-O- (DPPG tail group) (blue curve) for DPPG. [19] Upon polymer interaction, all the three modes showed softening (decrease in frequency) indicating that all the three polymers interact with phosphate region of DPPG. It is interesting to note that 1100 cm^{-1} vibrational mode splits into doublet upon interacting with AC3P and EC3P (Fig. 4.3B) along with softening. O=P-O$^-$ can conjugate hence has

the ability to resonate, hence the Fermi resonance (expected in AB_2) doublet does not exist in PO_2^- of DPPG (Fig. 4.3B). But upon addition of all three polymers, the electrostatic interaction with DPPG would affect the otherwise degenerate PO^{2-} vibration leading to splitting.

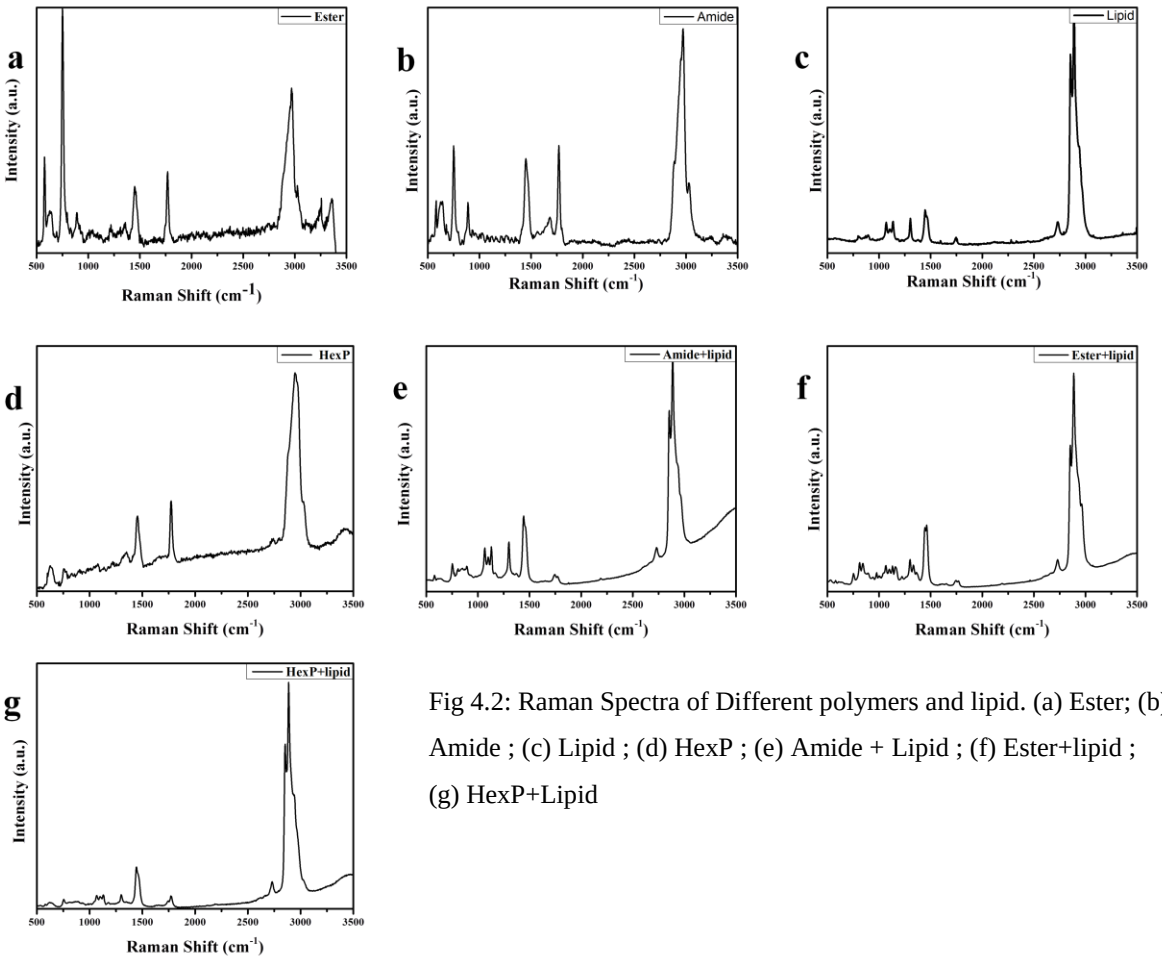

Fig 4.2: Raman Spectra of Different polymers and lipid. (a) Ester; (b) Amide ; (c) Lipid ; (d) HexP ; (e) Amide + Lipid ; (f) Ester+lipid ; (g) HexP+Lipid

HexP has less chance for hydrogen bonding with DPPG and hence the non-directional electrostatic interaction is weaker with no splitting of PO_2^- vibration (Fig. 4.3B). The hydrogen bonding ability of AC3P and EC3P with DPPG gets the cationic nitrogen localized in space leading to strong interactions with the PO_2^- group resulting in its splitting.

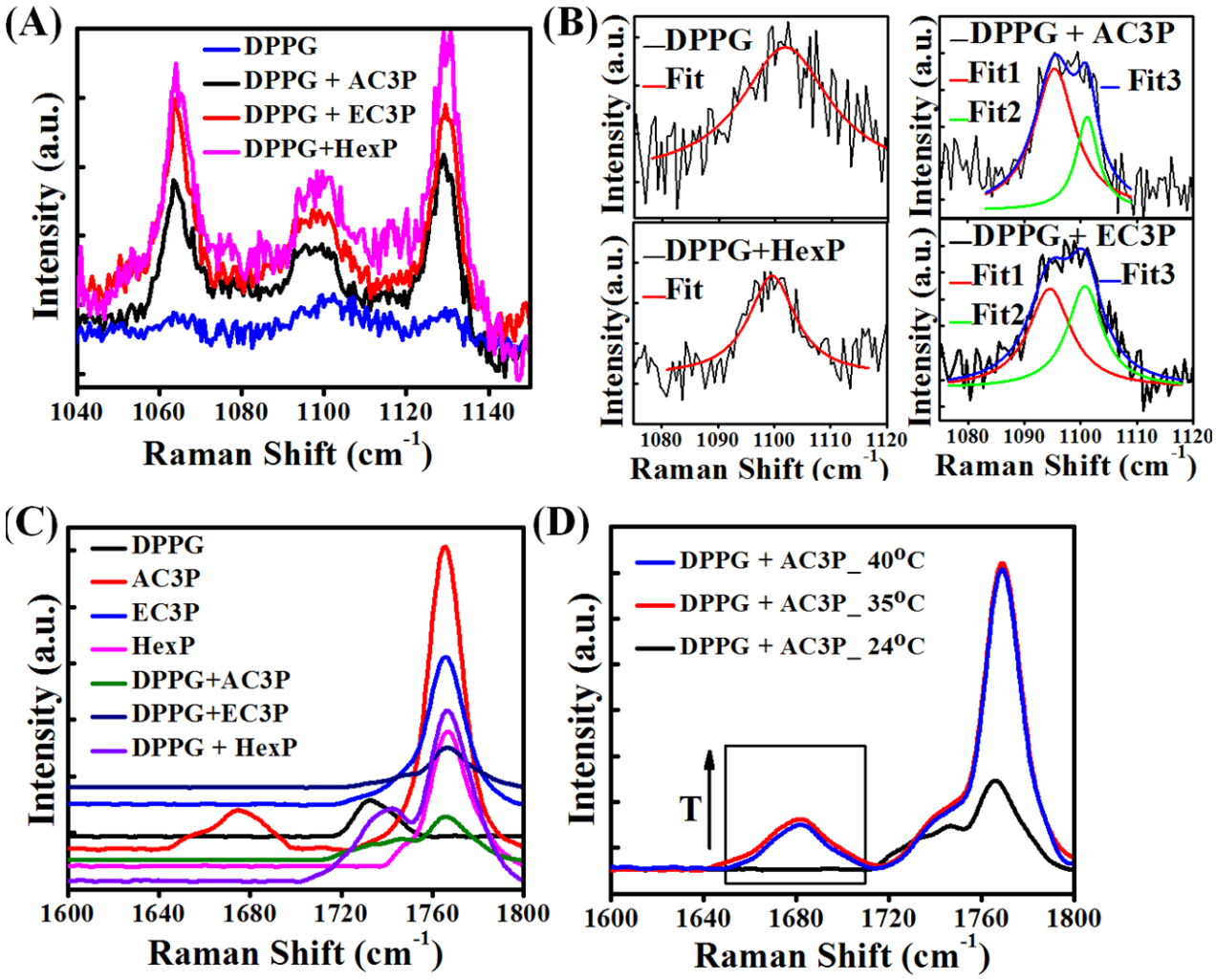

Figure 4.3. Polymer interactions with bacterial membrane lipid, DPPG using Raman spectroscopy. (A) Lipid phosphate vibrational modes (1064 cm^{-1}, -P-O- (DPPG head group), 1100 cm^{-1}, PO_2^- and 1129 cm^{-1}, -P-O- (DPPG tail group) DPPG and polymer + DPPG indicate softening (decrease in frequency) of all three modes. (B) Splitting of PO_2^- mode into a doublet (loss of degeneracy) due to strong interactions of amide polymer with DPPG, followed by weak interactions of ester polymer with DPPG and weaker interaction of HexP with DPPG. (C) Spectra in the region of 1600-1800 cm^{-1} showing side chain amide I vibration (1680 cm^{-1}) and the side chain ester C=O vibrational mode (1740 cm^{-1}), long chain ester C=O of DPPG (black curve) and polymer backbone C=O (imide) at around 1770 cm^{-1}. Upon interaction with DPPG, amide I mode (1680 cm^{-1}) of AC3P (red curve) disappears in DPPG + AC3P (green curve). (D) Temperature dependent spectra of DPPG + AC3P showing the emergence of amide I mode at high temperatures showing the strong hydrogen bonding between AC3P and DPPG.

The lower frequency mode is due to the PO- group (1096 cm^{-1}) and the higher frequency mode is due to the P=O group (1100 cm^{-1}). Interestingly, the relative intensities of the

two peaks in doublet is higher in AC3P + DPPG than in EC3P + DPPG suggesting the strong interactions of amide polymer with the lipid compared to the ester polymer (Fig. 4.2B). The polymer region (1600-1800 cm^{-1}) of the spectra as shown in Fig. 4.2C is dominated by the side chain amide I vibration (1680 cm^{-1}) and the side chain ester C=O vibrational mode (1740 cm^{-1}). [19, 20] This region is affected by the presence of a strong signature from the long chain ester C=O of DPPG (black curve Fig. 4.2C) and also from the polymer backbone C=O (imide) at around 1770 cm^{-1}. It is interesting to see that amide I mode (1680 cm^{-1}) disappears in DPPG + AC3P (green curve Fig. 4.2C) and looks very similar to the DPPG + EC3P spectrum (dark blue curve Fig. 4.2C). This is very important because it shows there is a strong hydrogen bonding between the amide moiety of AC3P and DPPG. It is interesting to see that the spectrum for DPPG + HexP (purple curve Fig. 4.2C) more or less looks like the convolution of DPPG (black curve, Fig. 4.2C) and HexP (magenta curve Fig. 4.2C). The long chain lipid ester (1740 cm^{-1}) peak has shifted showing some weak interaction between DPPG and HexP as observed earlier.

In order to confirm the hydrogen bonding, the Raman spectra for DPPG + AC3P was recorded on heating up to 40 °C (Phase transition temperature (T_m) of DPPG is 41 °C) (Fig. 4.3D). The emergence of amide (1680 cm^{-1}) band above 35 °C suggested the breaking of hydrogen bond. As a control the same regions were checked for Ester and Lipid (Fig 4.4 A and D) case and it was observed that no such peak starts to appear after heating. This confirms that amide residue is strongly interacting with lipid in DPPG and AC3P interaction. The strong 1740 cm^{-1} also shows the emergence of long chain ester C=O vibration of the lipid. Similar experiments in the DPPG + EC3P spectrum bring the emergence of a strong 1740 cm^{-1} similar to DPPG + AC3P indicated the breaking of ester polymer C=O hydrogen bond with DPPG (Fig. 4.4). Heating effect on the 1100 cm^{-1} mode showed no changes in DPPG and DPPG + HexP, but in DPPG + AC3P as well as DPPG + EC3P, the splitting still persisted suggesting that the molecules are still weakly hydrogen bonded and in position (Fig. 4.4C and F).

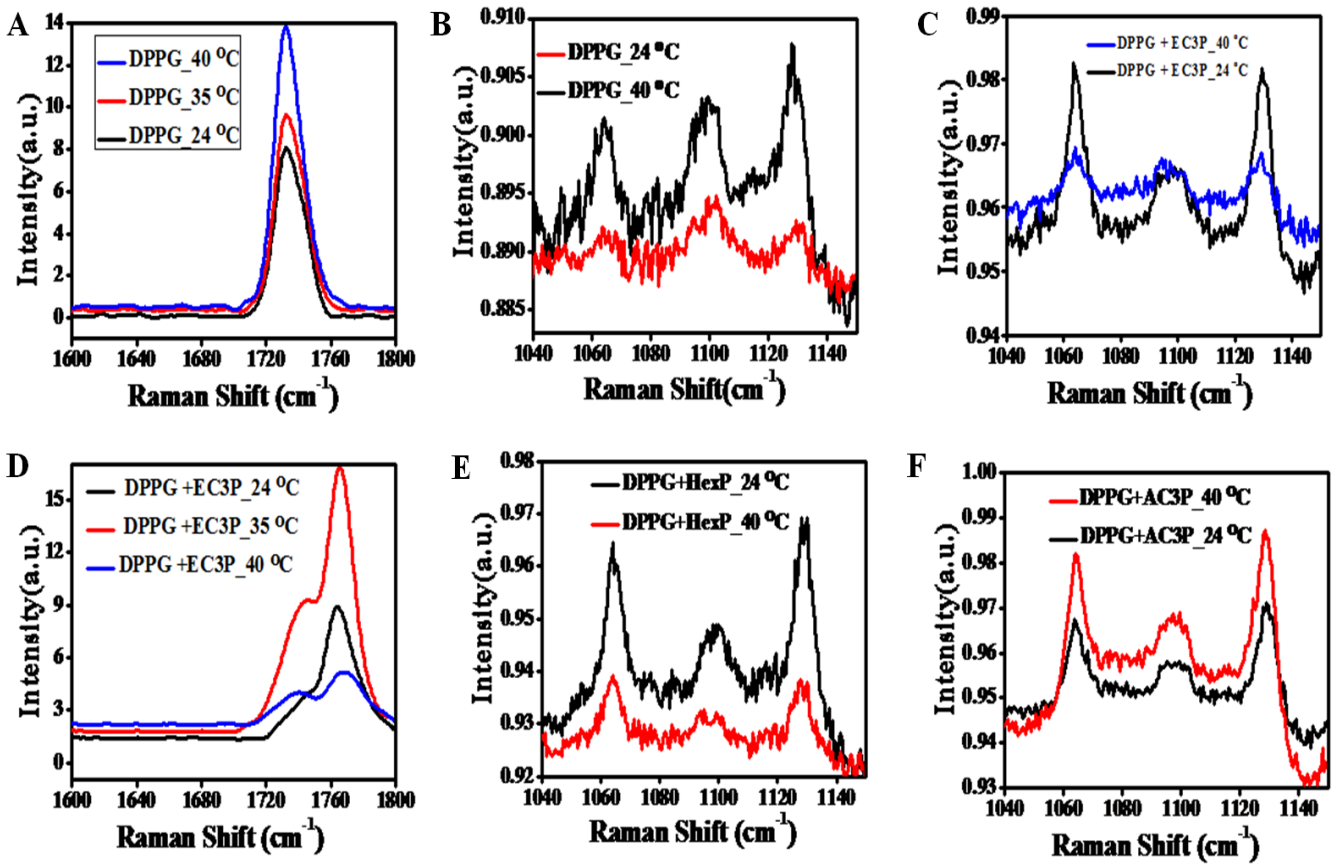

Figure 4.3-Temperature dependent Raman spectra of polymer and lipid and their mixers. (A) Lipid vibrational modes (amide region) with different temperature conditions. (B) Lipid phosphate region with temperature dependence. (C) Lipid and ester interaction in phosphate region with different temperatures. (D) Lipid and ester interaction in amide region with different temperatures. (E) Temperature dependent spectra of Lipid and HexP interaction in phosphate region. (F) Temperature dependent spectra of Lipid and amide interaction in phosphate region.

The above results clearly suggests that the difference between the interaction of AC3P and EC3P with DPPG is that the amide provides strong hydrogen bonding interactions with DPPG compared to EC3P probably through the two hydroxyl groups of the DPPG head group. These results also correlated with MD simulations which showed the hydrogen bonding interactions of amide polymers with the hydroxyl and phosphate oxygen atoms of POPG in bacterial model lipid bilayers. [21] Taken together, these data suggested that despite similar electrostatic interactions, the lack of strong hydrogen bonding interactions can render weaker binding of ester polymers with lipid bilayers compared to amide polymers.

4.4 Conclusion

Raman Spectroscopy is very useful tool to study the hydrogen bonding. Here we were successful in distinguishing the difference in hydrogen bonding between three polymers differing in functional groups (ester, amide and no functional group) binding to the lipid layer of bacteria. This would be very important in the development of the effective drug for antibiotics.

References

[1]. M. McKenna, *Nature*, 2013, 499, 394-396.

[2]. G. Taubes, *Science*, 2008, 321, 356-361.

[3]. R. E. Hancock and H. G. Sahl, *Nat. Biotechnol.*, 2006, 24, 1551-1557.

[4]. K. A. Brogden, *Nat. Rev. Microbiol.*, 2005, 3, 238-250.

[5]. M. Zasloff, *Nature*, 2002, 415, 389-395.

[6]. W. C. Wimley, *ACS Chem. Biol.*, 2010, 5, 905-917.

[7]. M. R. Yeaman and N. Y. Yount, *Pharmacol. Rev.*, 2003, 55, 27-55.

[8]. Y. Shai, *Biochimi. Biophys. Acta*, 1999, 1462, 55-70.

[9]. V. Yarlagadda, S. Samaddar, K. Paramanandham, B. R. Shome and J. Haldar, *Angew Chem Int Ed Engl*, 2015, 54, 13644-13649.

[10]. C. Krumm, S. Harmuth, M. Hijazi, B. Neugebauer, A. L. Kampmann, H. Geltenpoth, A. Sickmann and J. C. Tiller, *Angew Chem Int Ed Engl*, 2014, 53, 3830-3834.

[11]. F. Sgolastra, B. M. Deronde, J. M. Sarapas, A. Som and G. N. Tew, *Acc. Chem. Res.*, 2013, 46, 2977-2987.

[12]. M. S. Ganewatta and C. B. Tang, *Polymer*, 2015, 63, A1-A29.

[13]. H. Takahashi, E. F. Palermo, K. Yasuhara, G. A. Caputo and K. Kuroda, Macromol. *Biosci.*, 2013, 13, 1285-1299.

[14]. R. H. Liu, X. Y. Chen, S. Chakraborty, J. J. Lemke, Z. Hayouka, C. Chow, R. A. Welch, B. Weisblum, K. S. Masters and S. H. Gellman, *J. Am. Chem. Soc.*, 2014, 136, 4410-4418.

[15]. P. Li, C. Zhou, S. Rayatpisheh, K. Ye, Y. F. Poon, P. T. Hammond, H. Duan and M. B. Chan-Park, *Adv Mater*, 2012, 24, 4130-4137.

[16]. F. Nederberg, Y. Zhang, J. P. Tan, K. Xu, H. Wang, C. Yang, S. Gao, X. D. Guo, K. Fukushima, L. Li, J. L. Hedrick and Y. Y. Yang, *Nat. Chem.*, 2011, 3, 409-414.

[17]. V. Sambhy, B. R. Peterson and A. Sen, *Angew Chem Int Ed Engl*, 2008, 47, 1250-1254.

[18]. M. S. Ganewatta and C. B. Tang, Polymer, 2015, 63, A1-A29. 20. H. Takahashi, E. F. Palermo, K. Yasuhara, G. A. Caputo and K. Kuroda, *Macromol. Biosci.*, 2013, 13, 1285-1299.

[19]. Z. Movasaghi, S. Rehman and I. U. Rehman, *Appl Spectrosc Rev*, 2007, 42, 493-541.

[20]. H. H. Mantsch, A. Martin and D. G. Cameron, *Biochemistry*, 1981, 20, 3138-3145.

[21]. Uppu, Divakara; Konai, Mohini; Baul, Upayan; **Singh, Priyank**; Siersma, Tjalling ; Samaddar, Sandip; Hoque, Jiaul; Krishnamoorthy, Paramanandham; Vemparala, Satyavani; Hamoen, Leendert ; Shome, Bibek; Narayana, Chandrabhas; Haldar, Jayanta. Isosteric Substitution in Cationic-amphiphilic Polymers Reveals an Important Role for Hydrogen Bonding in Bacterial Membrane Interactions. (communicated, 2016)

Chapter-5

Raman Imaging of Himalayan Rocks

5.1 Introduction

Himalaya is a monument of great importance from spiritual as well as geographical point of view. The formation of Himalaya has been a centre of attraction for geologists. Forty million years ago, the continent of India, which was being carried northward by the Indo-Australian plate, collided with Asia. Since the initial encounter, the subcontinent of India has moved 2,000 kilometers farther north at a rate of 5 centimeters a year, sliding beneath Asia as it moves. The minerals present in the rocks have great details about the natural phenomenon that occurred at the time of this impact between the plates. Nagaland being at the edge of the Indo-Australian plate has plenty of information regarding the impact. Samples around Nagaland have been studied very well by Ghose et al [1].

Detached outcrops of Ophiolitic rocks along the east–west Indus–Tsangpo suture in the western Himalayas at the northern part of the Indian Plate bordering Tibet swerve around the eastern Himalayan syntaxis and continue southward along the Indo–Myanmar Ranges (IMR) and the Andaman–Nicobar Islands at the eastern margin of the Indian Plate. The rocks buried in this region carry quite crucial information of the conditions of impact of the Indo-Australian and Eurasian plate. Almost every report has claimed the existence of Glaucophane-bearing Eclogite which indicate that the thermodynamic conditions shall be low temperature and high pressure. Recent studies have shown the existence of Pyroxene which indicates the existence of Coesite phase as well. [1] The existence of Coesite gives the signature of ultra high pressure. This will definitely contribute to our better understanding of the natural phenomenon. Due to obvious limitations, EPMA studies were unable to probe for Coesite phase in the sample. Probable speculations for EPMA unable to detect Coesite phase is that the size of the Coesite crystals are too small. Raman spectroscopy being one of the important tools for molecular probing is very crucial for such critical studies.

5.2 Experimental

Samples were collected from Nagaland (Kohima) region of India shown in fig.5.1.

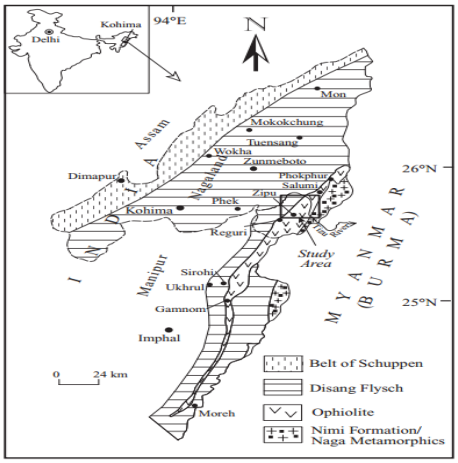

Fig. 5.1 Location of Sample

A thin film of few hundred microns was made out of the rocks by Geophysical society of India. Substrate used was glass sheet. Diamond polishing was done to ensure the stability of thin film. Dimensions of the samples were almost 2.54 cm * 1.5 cm. To ensure the presence of silica polymorph of quartz, i.e. Coesite, Raman images were recorded at several regions of the samples. Typical integration time for recording Raman spectra at each point is 0.6 seconds.

Confocal Raman (WiTec, Germany) setup was used to perform Raman spectroscopy and Raman Imaging measurements. Laser wavelength of 532 nm was used as the excitation source. Laser power at the sample was around 20 mW. The 60 X Nikon objectives with 0.8 NA was used for focussing the laser and collecting the Raman signals. UHTS600 SMFC spectrograph with CCD-17531 is the heart of the Raman system used. Raman spectra were collected at different spots to see the compositions. Based on these inputs characteristic peaks of different mineral phases were selected to make the Raman image of the region of interest.

5.3 Results and Discussions

Ghose *et al* have already reported a few phases in this sample such as Garnet, Epidote, Glaucophane, Aegirine, quartz etc, but the specific interest in doing Raman spectroscopy was to identify the Coesite phase of the SiO_2-polymorph. [1] Before discuss the observation of present investigation, let's discuss the Raman signatures of few important minerals. Since our interest is very specific to Coesite phase of quartz we'll

discuss their properties. The formation of quartz occurs at high pressure and relatively low temperatures (200-450°C). High pressure conditions give sufficient environment for Si-O bonds to form with relatively less stiffness. The bond vibration of Si-O in quartz is observed to be at around 465 cm^{-1}. [2] When the pressure goes higher the Si-O bond length squeezes and the vibrational frequency is shifted to 521 cm^{-1}. [2] This new structure is a polymorph of silica which is named as Coesite.

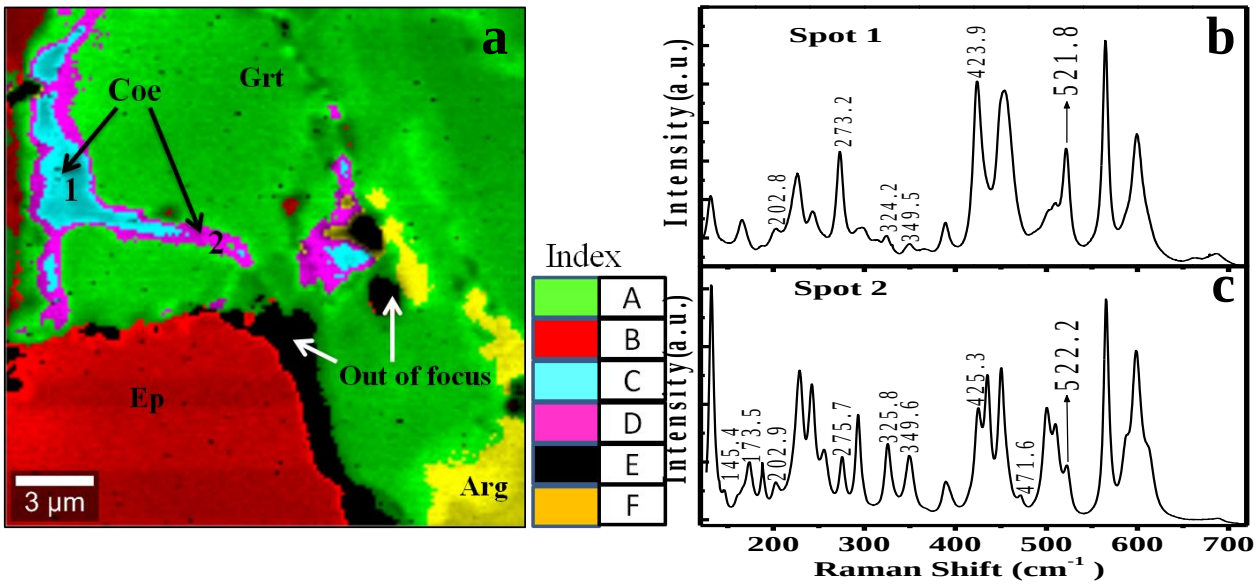

Figure 1(a). Raman image of the sample 139/80 –Eclogite, Naga Hills Ophiolite, India : A-Garnet-rich (918 cm^{-1}), B-Epidote-rich (455 cm^{-1}), C & D-Coesite-rich (522 cm^{-1} , observed) , E-Blank (Out of focus region), F- Aragonite-rich (1086 cm^{-1}); (b) Raman spectra of Coesite-rich region at Spot 1; (c) Raman spectra of Coesite-rich region at Spot 2

Knowing the signature peak of Coesite, Raman Spectroscopy becomes an appropriate tool for detecting the existence of Coesite in the sample 139/80. Information about the existence of Coesite phase would be helpful to understand the P-T conditions at which this was formed. In order to achieve the goal, Raman images were recorded at several regions using Raman spectrometer, details of which are given in experimental methods. Each Raman image contains the information of 20x20 μm^2 area.

The Raman map of the sample is represented in the Fig 1(a), using the characteristic peaks associated along with the intensities of Garnet, Epidote, Coesite and Aragonite. [2], [3], [4], [5] The black region shown in Figure 1(a) shows a flat Raman

spectrum because it was out of focus due to different level of the sample. It should be mentioned here that the various colored region in the Figure 1(a) are predominantly dominated by the mineral specified, but it has other minerals too in that region. Figure 1 (b,c) corresponds to the spectra obtained from the image of the sample (figure 1(a)). It is interesting that the intensity of various peaks of Coesite is reversed here. This is due to the birefringence property of Coesite. Since the laser light used in this case is polarized, the crystal orientation is different in the region C and D. The Raman depends on the polarizability of the system with respect to each vibration which is reflected in the intensity variation and sometimes could also be zero. Hence we believe that the region C and D are two orientations of the Coesite in the sample.

The strongest Raman signal of the Coesite is 521 cm^{-1} at ambient conditions. [2] We observe that this peak has shifted to 522 cm^{-1} (Figure 1 b,c). The increase is associated with the compressive stresses exerted by the surrounding garnet phase. Table 4.1 shows the various vibrational frequencies of the Coesite: [2]

Sr. No.	Coesite (cm^{-1}) (Reported)	Coesite (cm^{-1}) (observed)
1	151	145.4
2	176	173.5
3	204	202.8
4	269	275.7
5	326	325.8
6	355	349.6
7	427	425.3
8	466	471.6
9	521	522

Table 4.1 Raman frequencies of Coesite observed and reported.

The Raman mapping confirms the presence of the Coesite phase in the sample coexisting with the garnet and the epidote phases. There is also a strain exerted by the garnet and epidote on the Coesite suggesting a simultaneous formation of these phases.

5.4 Conclusion

In conclusion we have established the presence of Coesite phase in the sample which in turn leads to the fact that the initial impact conditions were high temperature and very high pressure (3-4 GPa). This information would be helpful in further investigating the origin of Himalaya and simulating such tectonic activities.

References

[1]. Ghose *et al.* Geological and mineralogical study of eclogite and glaucophane schists in the Naga Hills Ophiolite, Northeast India, *Island Arc* (2010) 19, 336–356.

[2]. Gillet *et al*, *J.Geophys.Res.* 95, 21635-21655 (1990).

[3]. Hofmeister, A.M., Chopelas, A., Phys. Chem. Minerals, 17, 503-526 (1991a)

[4]. P. Gillet, C. Biellmann, B. Reynard, and P. F. McMillan, Phys. Chem. Minerals, 20, 1-18 (1993)

[5]. http://rruff.info/Epidote/R100129 , Raman mineral Database.

Chapter-6

Raman optical activity instrumentation

6.1 Introduction

Present work deals with designing and setting up of Raman optical activity (ROA) spectrometer by modifying the existing Raman spectrometer. Chirality in molecules play very important role in their functioning. Especially biomolecules like proteins and DNA are highly sensitive to their specific Chirality. It is observed that naturally abundant proteins are outcome of L- amino acid chains whereas DNAs are outcome of polymerization of D conformer of the nucleic acids. Importance of Chirality is evident from the fact that a few protein stop functioning over the period of time because of change is Chirality of few amino acid residues. This specific phenomenon is called Chirality shifting. Raman spectroscopy is proven to be tool of great importance for studying biomolecules. [1-4] But it does not provide sufficient Chirality information. In 1969, L.D. Barron observed that if the Raman scattering is recorded by using circularly polarized light (left and right circular polarization); the intensity in each case doesn't remain same. [5] He realized that this case is particular to optically active materials, which indicate that measuring the difference could give information about the Chirality of the system. Based on reported literature a successful attempt to fabricate the ROA setup was made. [6-8]

ROA measures a small difference in the intensity of vibrational Raman scattering from chiral molecules in right- and left-circularly polarized (RCP and LCP respectively) incident light; equivalently, the intensity of a small circularly polarized component in the scattered light, using incident light of fixed polarization. These two approaches to measure ROA are named as incident circular polarization (ICP)-ROA and scattered circular polarization (SCP)-ROA respectively.

There are several ways to go about such measurements like use of lock in amplifiers can help us in enhancing the signal to noise ratio which in turn will make the ROA spectra cleaner. [8] It is reported that artifacts can easily affect the ROA signal, to make sure that recorded data is artifact free (or to make sure the signal to be ROA signal) following should be checked.

- Reproducibility of ROA spectra: The signal should be reproducible to make sure that the signal is not artifact.
- The ROA spectra of L conformer of the sample must be negative of ROA spectra of D conformer of the same sample.

There are two possibilities of ROA measurements: [6] ICP ROA and SCP ROA as shown in Fig. 6.1. ICP ROA invokes the circular polarization to be incident at the sample whereas the SCP ROA measures the circularly polarized components in the scattered light.

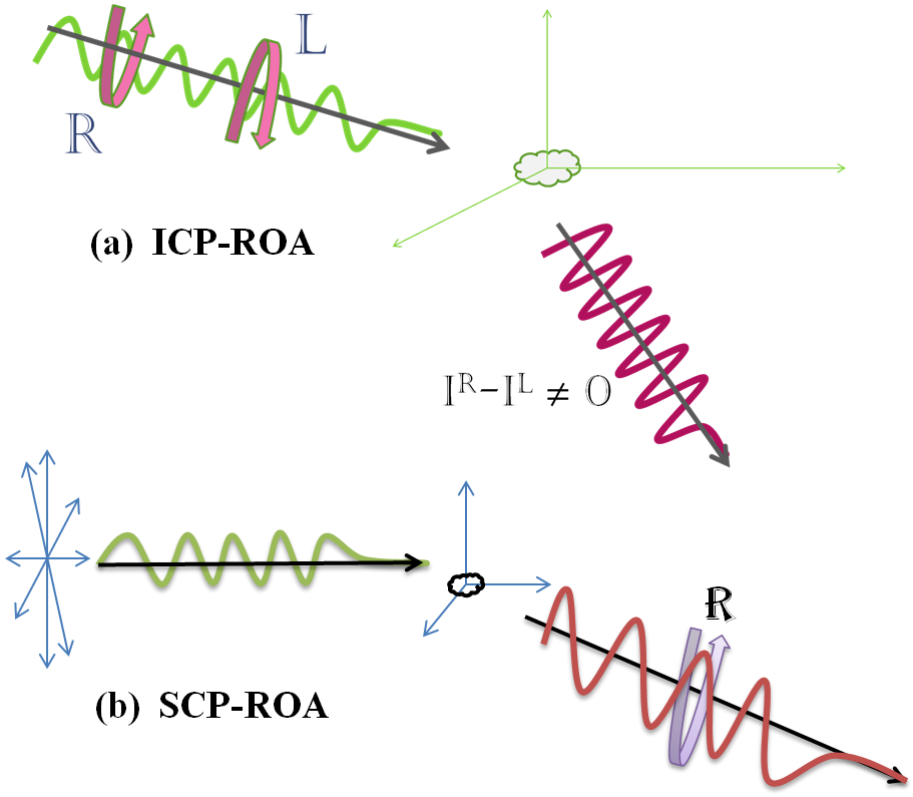

Fig.6.1-Two equivalent ROA measurement geometry. (a) ICP-ROA geometry, Incident beam is made circularly polarized and Raman spectra is recorded for each Left and Right circular polarization and the difference (I^R-I^L) is observed. (b) SCP-ROA geometry, Right and left circularly polarized components of scattered beam is observed and difference (I_R-I_L) is measured.

6.2 Experimental

In the present attempt to modify the existing setup (Fig 2.2), ICP-ROA approach is used. As it is mentioned that ROA is very small effect, the perfection in producing the circularly polarized light plays very crucial role to measure ideal ROA spectra. Basic optics, quarter wave plate and linear polarizer were used to produce near to perfect circular polarization.

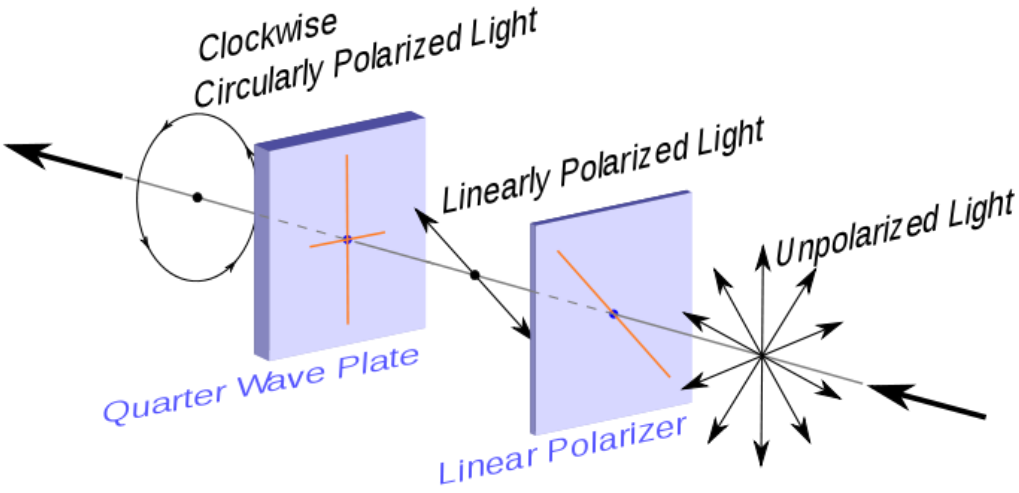

Fig. 6.1- Schematic diagram of generation of circular polarization using quarter wave plate and linear polarizer

When the plane of polarization of polarizer orients $+\pi/4$ with optic axis of quarter wave plate the outcome light has right circular polarization. If the angle between plane of polarization of polarizer and optic axis of quarter wave plate is $-\pi/4$, the out coming light is left circular polarized (Fig. 6.1). In all other angles the out coming light will be elliptically polarized. To test the circularity of the output, another linear polarizer (analyzer) is inserted after the quarter wave plate. If the circularly polarized light has been produced by quarter wave plate then the intensity of light coming out of the analyzer is independent of the orientation of its plane of polarization.

It was observed that the existing laser is not plane polarized; a linear polarizer was used to polarize the light to maximum possible extent, a quarter wave plate (polymer based quarter wave plate with 10% tolerance) was inserted in the path after the linear polarizer. Since the direction of optic axis was unknown, a random orientation was made.

An analyzer was inserted to check the perfection of circular polarization achieved. A power meter was placed to check the intensity of output beam. Analyzer was rotated by 360° and the power meter reading was checked. Varying the orientation of quarter wave plate, a condition with minimum fluctuation in power meter (for all the orientations of analyzer) was achieved. The circular polarization achieved in this way is left circular polarization. To achieve right circular polarization, the quarter wave plate was rotated by $\pi/2$ angle.

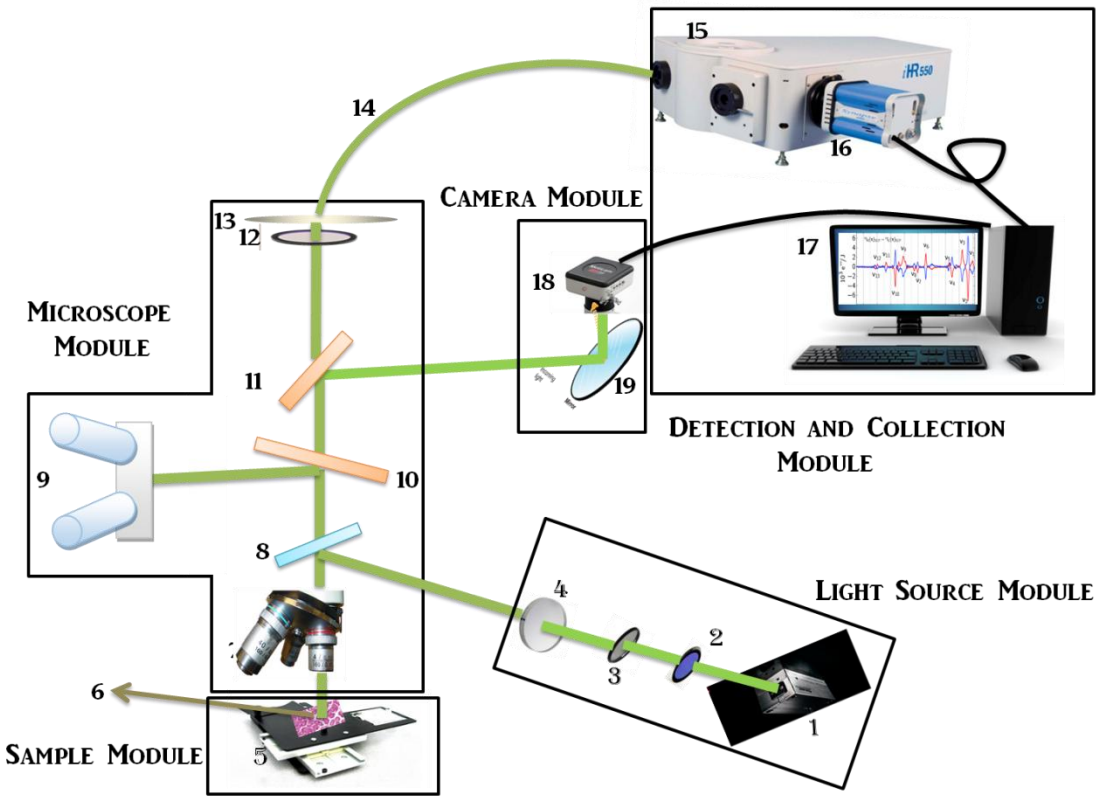

Figure 6.2- Schematic of ROA setup for demonstration. 1-laser light Source; 2- Band pass filter; 3- Linear Polarizer; 4- Quarter wave plate; 5-Sample Stage; 6-Sample;7-Objective lens; 8-Special Mirror; 9-Binocular; 10,11-Beam Splitter; 12-Edge Filter; 13-Focussing lens; 14-Optical Fiber; 15-Spectrometer; 16-CCD; 17-Computer; 18-Camera; 19-Mirror.

Once the circular polarization is achieved, laser is aligned with Monochromator and CCD. The alignment procedure is given in chapter 2. ROA setup designed is shown in Fig. 6.2. Insertion of extra optical components reduces the power of the output beam so

the scattering efficiency goes down. To make sure that the spectra recorded in such a way is strong enough, almost 100-500 spectra were recorded for same circular polarization and then the sum of them was taken as final Raman spectra (left and right circular polarization each). Manual subtraction of Raman spectra by RCP light and LCP light was done. The process was repeated with D and L conformer of the sample used, which is phenylalanine. The experimental data was reproduced 4-5 times and ROA spectra were compared. A high rate of reported ROA signal was achieved. There were many artifacts observed in the final spectra.

6.3 Results and Discussions

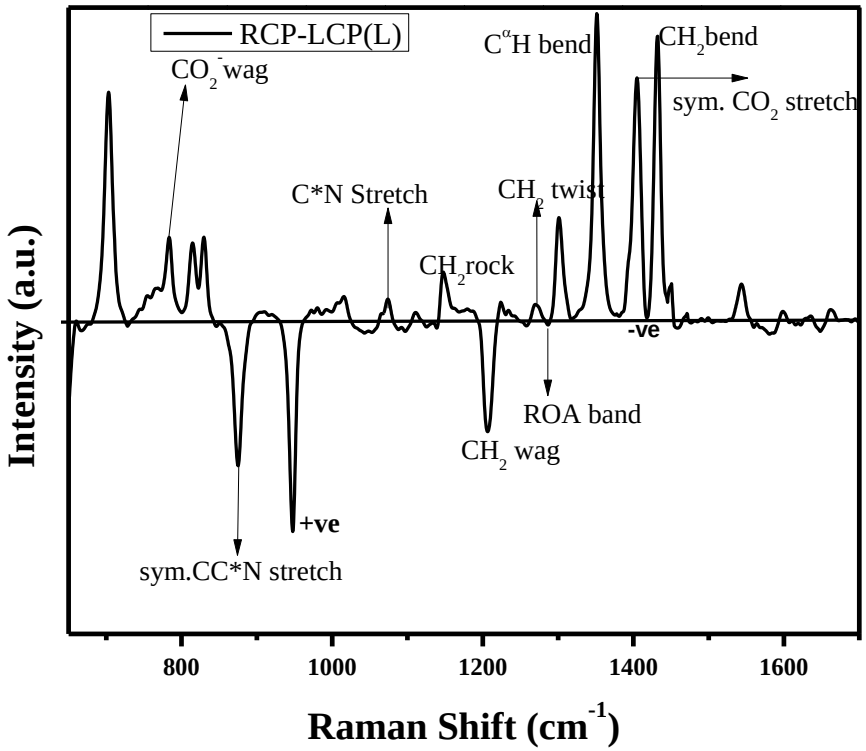

Figure 6.3- ROA spectrum of L- Cysteine.

Figure 6.3 shows the ROA spectra for L-cysteine by subtracting the Raman spectra obtained from RCP and LCP light. Band assignments were done on the basis of literature reports. [9] The ROA spectrum of L-cysteine was matching well with the reported data. There are a few artifacts observed in the present investigation, which is because of

imperfections in generation of circularly polarized light. Results were found to be reproducible (artifacts were confirmed by reproducibility check). Due to non availability of D-cysteine the ROA was not performed on D-cysteine.

In order to check the proof of principle for ROA setup, we used phenylalanine**.** Figure 6.4 shows the ROA spectra of L and D conformers of Phenylalanine. We verified the spectrum of L and D phenylalanine which follows the second check. This ensures that the setup shows the proof of principle.

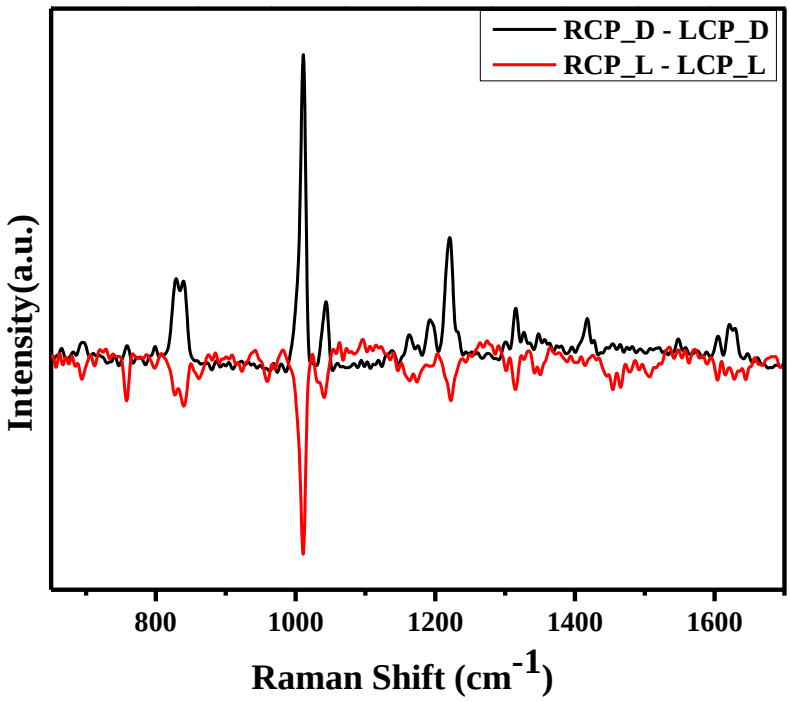

Figure 6.4- ROA spectra of L and D conformer of Phenylalanine

The setup worked very fine for demonstration purpose but there are several issues with the designed setup.

- The setup included a laser of 5 mW, the power of which went down to 0.5 mW at the sample after insertion of quarter wave plate and linear polarizer. This power was much less for probing samples of research interest. To solve this we have to increase the laser power to ~200mW. For demonstration purpose this

problem was circumvented by taking 400-500 spectra of each circular polarization and then averaged.

- Another issue with laser was the stability, which plays a crucial role for giving artifacts. Since ROA spectra is outcome of subtraction, stability is a must condition for both RCP and LCP light. A highly stable laser would avoid such problem. This would cause artifacts in spectra.
- The tolerance level of polymer quarter wave plate was 10% which increases the imperfection in the circular polarization of the output light and consequently perturbing the actual ROA spectrum with artifacts.
- Manual errors: The orientation of quarter wave plate was managed manually which would directly affect the circularity of the polarization state. To fix this problem we need to replace the quarter wave plate by Electro optic modulator, which would precisely modulate the polarization state of the incident light.
- Post analysis: Post analysis is another big reason for artifacts, all the analysis is done manually so human error is expected. To avoid this, many spectra were recorded and the sum spectrum was considered as final spectra. To avoid this in the final setup we have proposed a triggering mechanism and Lab view program which would collect 1000s of spectra for each of the circular polarization and produce the output as average of them.

6.4 Conclusion

A successful attempt to demonstrate proof of principle for the ROA spectrometer was made. The testing of the fabricated spectrometer gives satisfactorily matching results with literature. There are several questions to be addressed such as increment in S/N ratio and automated subtraction of the Raman spectra etc. Further development would add to final version of the setup.

References

[1]. D. Karthigeyan, S. Surabhi, Pushpak Mizar, S. Soumik, Amrita Banerjee, Sarmistha H. Sinha, Dipak Dasgupta, Chandrabhas Narayana and Tapas K. Kundu, A Dual Non-ATP Analogue Inhibitor of Aurora Kinases A and B, Derived from Resorcinol with a Mixed Mode of Inhibition, *Chemical Biology and Drug Design* (2016).

[2]. Soumik Siddhanta, Ishan Barman and Chandrabhas Narayana, Revealing the trehalose mediated inhibition of protein aggregation through lysozyme–silver nanoparticle interaction, *Soft Matter* **11**, 7241 – 7249 (2015).

[3]. Dhanasekaran Karthigeyan, Soumik Siddhanta, Annavarapu Hari Kishore, Sathya S R R Perumal, Hans A Agren, Surabhi Sudevan, Akshay V. Bhat, Karanam Balasubramanyam, Rangappa Kanchugarakoppal Subbegowda, Tapas K Kundu and Chandrabhas Narayana, SERS and MD simulation studies of a kinase inhibitor demonstrate the emergence of a potential drug discovery tool, *Proceedings of the National Academy of Sciences (USA)* **111**, 10416 – 10421 (2014).

[4]. George J. Thomas, Jr., Raman Spectroscopy of protein and nucleic acid assemblies, *Annual Review of Biophysics and Biomolecular Structure*, (1999).

[5]. Rayleigh and Raman scattering from optically active molecules. L. D. Barron and A. D. Buckingham (1971). *Mol. Phys.* **20**, 1111-1119.

[6]. Lutz Hecht, Laurence D. Barron, Ewan W. Blanch, Alasdair F. Bell and Loren A. Day, Raman Optical Activity Instrument for Studies of Biopolymer Structure and Dynamics, *J. Raman Spectrosc*. 30, 815–825 (1999).

[7]. Laurence D. Barron , Lutz Hecht , Iain H. McColl & Ewan W. Blanch, Raman optical activity comes of age, *Molecular Physics*, 2006.

[8]. Laurence A. Nafie, Infrared and Raman vibrational optical activity: Theoretical and Experimental Aspects, *Annual Review of Physical Chemistry*, 1997.

[9]. A. R. Gargaro, L. D. Barron and L. Hecht, Vibrational Raman optical activity of simple amino acids, *J.Raman Spec*., 1993.

Chapter-7

Future Scope

Raman spectroscopy is very versatile tool to get several type of information. Starting from chemical bonding to properties like ferroelectricity, Chirality etc. can be probed. As discussed in chapter 3 there can be studies related to structural phase transitions which could give us the information about dielectric properties. Use of Raman scattering has played very important role in understanding the Bio-molecular interactions as well. Present work opens up gates for in-vivo studies of membrane-drug and several other bio-molecular interactions.

The proof of principle shown in chapter 6 gives enormous scope for further development of ROA spectrometer (Proposed setup in Fig7.1 given below) which has several advantages over the (Circular Dichroism) CD spectroscopy for exploring higher order structures in proteins, DNAs etc. This setup in its final version would be a great deal of getting various information out of biological molecules, supramolecular assemblies etc. ROA spectra of Protein or supramolecules provide information on the secondary and tertiary structures of the polypeptide backbone, hydration, side-chain conformation, and structural elements present in denatured states. There have been several reports in literature mentioning the structures of proteins and viruses by using ROA technique.

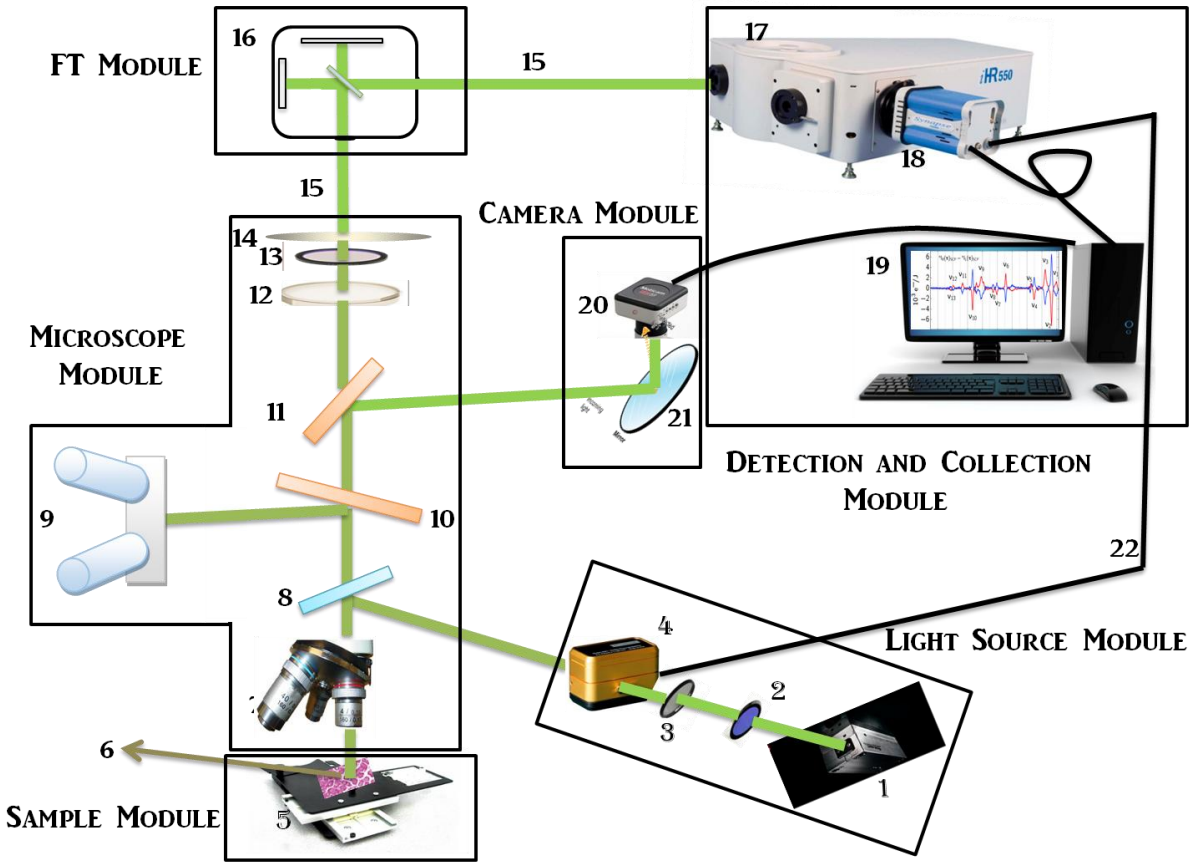

Figure7.1: - Schematic of Proposed FTROA Spectrometer

1-laser light Source; 2- Band pass filter; 3- Neutral density filter; 4- EOM; 5-Sample Stage; 6-Sample;7-Objective lens; 8-Special Mirror; 9-Binocular; 10,11-Beam Splitter; 12-Scrambler; 13-Edge Filter; 14-Focussing lens; 15-Optical Fiber; 16-Michelson Interferometer; 17-Spectrometer; 18-CCD; 19-Computer; 20-Camera; 21-Mirror; 22-EOM trigger